CRYSTALLIZATION OF AMORPHOUS GE THIN FILMS BY NANOSECOND PULSED INFRARED LASER

A THESIS SUBMITTED TO
THE GRADUATE SCHOOL OF NATURAL AND APPLIED SCIENCES
OF
MIDDLE EAST TECHNICAL UNIVERSITY

BY

CEREN KORKUT

IN PARTIAL FULFILLMENT OF THE REQUIREMENTS
FOR
THE DEGREE OF MASTER OF SCIENCE
IN
PHYSICS

JANUARY 2023

Approval of the thesis:

CRYSTALLIZATION OF AMORPHOUS GE THIN FILMS BY NANOSECOND PULSED INFRARED LASER

submitted by **Ceren KORKUT** in partial fulfillment of the requirements for the degree of **Master of Science** in **Physics, Middle East Technical University** by,

Prof. Dr. Halil Kalıpçılar
Dean, Graduate School of **Natural and Applied Sciences** ________________

Prof. Dr. Seçkin Kürkcüoğlu
Head of the Department, **Physics** ________________

Prof. Dr. Alpan Bek
Supervisor, **Physics, METU** ________________

Assist. Prof. Dr. Kamil Çınar
Co-Supervisor, **Physics, Gebze Technical University** ________________

Examining Committee Members:

Prof. Dr. Raşit Turan
Physics, METU ________________

Prof. Dr. Alpan Bek
Physics, METU ________________

Assist. Prof. Dr. Ihor Pavlov
Physics, METU ________________

Assoc. Prof. Dr. Tahir Çolakoğlu
Physics Engineering, Ankara Uni. ________________

Assist. Prof. Dr. Kamil Çınar
Physics, Gebze Technical Uni. ________________

Date: 20.01.2023

I hereby declare that all information in this document has been obtained and presented in accordance with academic rules and ethical conduct. I also declare that, as required by these rules and conduct, I have fully cited and referenced all material and results that are not original to this work.

Name Last name : Ceren Korkut

Signature :

ABSTRACT

CRYSTALLIZATION OF AMORPHOUS GE THIN FILMS BY NANOSECOND PULSED INFRARED LASER

Korkut, Ceren
Master of Science, Physics
Supervisor: Prof. Dr. Alpan Bek
Co-Supervisor: Assist. Prof. Dr Kamil Çınar

January 2023, 60 pages

Crystalline semiconductors have superior optical and electrical properties to an amorphous structure; therefore, they are an essential part of photovoltaic applications. Pulsed laser irradiation is a cost-effective technique for the growth of polycrystalline germanium (pc-Ge). Laser processing also enables the production of local and wide-ranging nano-crystalline surface structures. Germanium has high carrier mobility, and Ge nanocrystals and microcrystals have a great potential in optoelectronics applications due to their optical properties. Laser parameters such as laser fluence and scan speed play an essential role in forming well-aligned and oriented pc-Ge domains. In this thesis, the nanosecond pulsed infrared laser parameters are investigated to form high-quality crystal structures. Besides, with the improvement of line focus scanning optics and different deposition techniques of Ge thin films, the dominant mechanism of crystallinity, and defect formation on the pc-Ge thin-films are studied. The laser crystallization is applied at room temperature in the air without additional heating substrates. The results of this study pave the way for producing crack-free and high-quality crystalline device-grade thin films, which may find applications in photovoltaics, and other thin film device applications.

Keywords: laser crystallization, germanium thin films

ÖZ

AMORF GE İNCE FİLMLERİN NANOSANİYE ATIMLI KIZILÖTESİ LAZER İLE KRİSTALİZASYONU

Korkut, Ceren
Yüksek Lisans, Fizik
Tez Yöneticisi: Prof. Dr. Alpan Bek
Ortak Tez Yöneticisi: Dr. Öğr. Üyesi Kamil Çınar

Ocak 2023, 60 sayfa

Kristal yarı iletkenler, amorf bir yapıya göre üstün optik ve elektriksel özelliklere sahiptir; bu nedenle, fotovoltaik uygulamaların önemli bir parçasıdırlar. Darbeli lazer ışınlaması, polikristal germanyum (pc-Ge) büyümesi için uygun maliyetli bir tekniktir. Lazer ile işleme ayrıca bölgesel ve geniş kapsamlı nanokristal yüzey yapılarının üretimini de sağlar. Germanyum yüksek taşıyıcı hareketliliğe sahiptir ve Ge nanokristaller ve mikrokristaller, optik özelliklerinden dolayı optoelektronik uygulamalarda büyük bir potansiyele sahiptir. Lazer akışı ve tarama hızı gibi lazer parametreleri, iyi hizalanmış ve yönlendirilmiş pc-Ge alanlarının oluşturulmasında önemli bir rol oynar. Bu tezde, yüksek kaliteli kristal yapılar oluşturmak için nanosaniye darbeli kızılötesi lazer parametreleri incelenmiştir. Ayrıca, çeşitli kalınlıklarda Ge tabakasının ve alttaşlarının, hâkim olan kristallik mekanizması ve pc-Ge ince filmler üzerinde kusur oluşumu incelenmiştir. Lazerle kristalizasyon, ilave ısıtma alttaşları olmaksızın oda sıcaklığında havada gerçekleştirilmiştir. Bu çalışmanın sonuçları, fotovoltaik ve diğer ince film cihaz uygulamalarında uygulama bulabilen, çatlaksız ve yüksek kaliteli kristalin cihaz kalitesinde ince filmler üretmenin yolunu açmaktadır.

Anahtar Kelimeler: polikristal germanyum, lazerle kristalizasyonu

“Dünyada her şey için; maddiyat için, maneviyat için, başarı için en hakiki mürşit ilimdir, fendir. İlim ve fennin haricînde mürşit aramak gaflettir, cehalettir, delalettir.”

“For everything in the world; The only true guide for materiality, spirituality and success is science. It is heedlessness, ignorance, and heresy to seek a guide other than knowledge and science.”

Mustafa Kemal Atatürk

ACKNOWLEDGMENTS

I would like to express my deepest gratitude to my supervisor Prof. Dr. Alpan Bek for his guidance, understanding and support through my Master's study. I am deeply thankful to my co-supervisor Assist. Prof. Dr. Kamil Çınar for sharing his knowledge, support, and encouragement.

I would also like to thank Assoc. Prof. Dr. Mustafa Kulakcı, Milad Ghasemi, Buse Ünlü and GÜNAM for the fabrication of germanium films.

I am also very grateful to Nanooptics Research Lab members, Nardin Avishan, Özge Demirtaş, Serena Nur Erkızan, Alp Akbıyık and Hüseyin Umut Tepe for their friendship and support. My deepest thanks also go to Buse Ünlü and Hande İşbilir for their energies and support whenever I need them.

I would like to express my deepest gratitude to Ekinfen family, Cengiz Bayıldıran, Ferdane Bayıldıran and İsmail Erdem Bayıldıran for supporting throughout my education.

I would like to extend my sincere thanks to my family, Şahin Korkut, Gülseren Korkut and Eren Korkut. They are always by my side in every kind of situation.

Finally, I would like to thank to my love, Mustafa Çakır for his support and love since prep class. I am so lucky to be with him.

I acknowledge the financial support from The Scientific and Technological Research Council of Turkey (TÜB˙ITAK) under grant numbers 119N413 and 115M061.

TABLE OF CONTENTS

ABSTRACT v

ÖZ vii

ACKNOWLEDGMENTS x

TABLE OF CONTENTS xi

LIST OF TABLES xiv

LIST OF FIGURES xv

LIST OF ABBREVIATIONS xvii

CHAPTERS

1 INTRODUCTION 1

1.1 Group IV Photonics Based on Germanium 1

1.2 Conventional Annealing Methods for Crystallization of Amorphous Germanium 3

1.3 Laser Crystallization of Amorphous Germanium Thin-Films 4

2 THEORETICAL BACKGROUND 7

2.1 Dynamics of Crystal Growth of Amorphous Germanium Thin-Films 7

2.2 Laser Induced Phase Transformation of Germanium 9

2.3 Explosive Crystallization of Amorphous Germanium Thin-Films 11

2.4 Raman Scattering 12

2.5 Raman-Strain Relations in Strained Germanium 14

3 IMPROVEMENT OF THE LINE FOCUS SCANNING OPTICS 19

3.1 Introducing of Laser Marking System 19

3.2 Gaussian Beam Profile by the Cylindrical Lens 19

3.3 Flat-Top Beam Profile by the Powell Lens 20

4 LASER CRYSTALLIZATION AND CHARACTERIZATION OF AMORPHOUS GERMANIUM THIN-FILMS DEPOSITED BY E-BEAM 25

4.1 Preparation of a-Ge Thin-Films 25

4.2 Laser Crystallization of a-Ge Thin-Films and Line Focus Scanning by the Cylindrical Lens 25

4.2.1 LC-Processed Regions with Non-Overlapping Pulses 26

4.2.1.1 Optical Microscope Images 26

4.2.1.2 Raman Analysis 27

4.2.2 LC-Processed Regions with Highly Overlapping Pulses 28

4.2.2.1 Optical Microscope and SEM Images 29

4.2.2.2 Raman and Tensile Stress Analysis 30

4.2.2.3 EBSD Images and Grain Size Distribution 34

4.2.2.4 XRD Spectrum 37

4.2.2.5 Absorbance Spectrum 39

5 LASER CRYSTALLIZATION AND CHARACTERIZATION OF AMORPHOUS GERMANIUM THIN-FILMS DEPOSITED BY SPUTTERING 41

5.1 Preparation of a-Ge Thin-Films 41

5.2 Laser Crystallization of a-Ge Thin-Films and Line Focus Scanning by the Cylindrical Lens 41

5.2.1 Optical Microscope, EBSD, SEM and Raman Measurement Results 41

5.3 Laser Crystallization of a-Ge Thin-Films and Line Focus Scanning by the Powell Lens 45

5.3.1 Optical Microscope, SEM and EBSD Measurement Results 45

6 CONCLUSION AND FUTURE WORK 49

REFERENCES 51

LIST OF TABLES

TABLES

Table 1.1 Achievements in the Literature 5

LIST OF FIGURES

FIGURES

Figure 1.1 Band structure of Ge and Si [11]. 3
Figure 1.2 Absorption coefficient vs wavelength graph for Si and Ge [12]. 3
Figure 2.1 Free energy vs temperature graph of a-Ge and c-Ge [35]. 8
Figure 2.2 Anti-stokes, rayleigh and stokes cattering [51]. 13
Figure 3.1 Laser marking system with a cylindrical lens. 20
Figure 3.2 Beam profile of the cylindrical lens and the Powell lens [72]. 20
Figure 3.3 A schematic view of the laser system with a Powell lens. 21
Figure 3.4 The streching length and apex diameter vs working distance graph..... 22
Figure 4.1 Optical microscope images of LC-processed regions with laser fluences of (a) 272 and (b) 416 mJ/cm^2 at a fixed scan speed of 4600 mm/s (non-overlapping pulses). 27
Figure 4.2 Raman analysis of LC processes regions with different laser fluences at a fixed scan speed of 4600 mm/s (non-
pulses). 28
Figure 4.3 Optical microscope images of LC of a-Ge with a laser fluences of 45, 68, 110 mJ/cm^2, respectively. 29
Figure 4.4 SEM images of the LC-processed regions with laser fluences of (a) 115 mJ/cm^2 and (b) 110 mJ/cm^2 with corresponding optical microscopy images in the insets. 30
Figure 4.5 Raman peak position and FWHM of the LC-Ge thin films as a function of the laser fluence with the scan speed of 5 mm/s... 31
Figure 4.6 Raman peak position and FWHM of the LC-Ge thin films as a function of scan speed at a laser fluence of 110 mJ/cm^2... 30
Figure 4.7 Raman spectra of a-Ge and LC-Ge thin films and c-Ge for reference. . 33
Figure 4.8 EBSD maps of the LC processed regions with laser fluences of (a) 45mJ/cm^2, (b) 110 mJ/cm^2 with color map and (c) the grain size distribution of 45 mJ/cm^2 and 110 mJ/cm^2. 35

Figure 4.9 The XRD patterns of the as-deposited and LC-Ge thin-films at laser fluences of 110 mJ/cm^2. 37
Figure 4.10 The bowing effect and differently stressed regions of LC Ge film . .. 37
Figure 4.11 The absorbance spectrum of a-Ge and LC-Ge thin-films with a thickness of 300 nm. 39
Figure 5.1 Optical microscope and SEM image of the LC-processed regions with the laser fluences of 53 mJ/cm^2 and scan speed of 5 mm/s. 40
Figure 5.2 Optical microscope and SEM image of the LC-processed regions with the laser fluences of 82 mJ/cm^2 and scan speed of 5 mm/s. 41
Figure 5.3 Raman spectra of the bulk-Ge and the LC-processed samples with laser fluences of 68 mJ/cm^2 and 82 mJ/cm^2 with the scan speed of 5 mm/s. 42
Figure 5.4 Optical microscope images of LC processed sputtered Ge region using (a) the cylindrical lens (b) their corresponding EBSD maps. 44
Figure 5.5 Optical microscope and EBSD images of the LC-Ge with a laser fluence of 54 mJ/cm^2 and a scan speed of 5 mm/s, respectively. 45
Figure 5.6 SEM and EBSD images of the LC-Ge with a laser fluence of 68 mJ/cm^2 and a scan speed of 5 mm/s, respectively. 46
Figure 5.7 SEM and EBSD images of the LC-Ge with a laser fluence of 72 mJ/cm^2 and a scan speed of 5 mm/s, respectively.. 47

LIST OF ABBREVIATIONS

ABBREVIATIONS	
Si	Silicon
Ge	Germanium
CMOS	Complementary-Metal-Oxide-Semiconductor
pc-Ge	Polycrystalline Ge
SPC	Solid Phase Crystallization
MIC	Metal-Induced Crystallization
IR	Infrared
CW	Continuous Wave
LC	Laser Crystallization
T_m	Melting Point
a-Ge	Amorphous Germanium
c-Ge	Crystalline Germanium
T_{ma}	Melting Point of a-Ge
T_{mc}	Melting Point of c-Ge
ε_i	Strain Components
Δw	The Shift in the Raman Peak Position
k	Linear Coefficient
ε	Tensile Stress
LO	Longitudinal Optical

TO	Transverse Optical
k_{TO}	Transverse Optical Linear Coefficient
ρ	Mass Density
T	Temperature
k	Thermal Conductivity
Q	Volumetric Heat Source
C_p	Specific Heat Capacity
R	Reflectivity
α	Absorption Coefficient

CHAPTER 1

INTRODUCTION

A short introduction to the roles and applications of crystalline germanium is given to in this chapter. Then, the conventional annealing and laser crystallization methods for crystallization of amorphous germanium is explained.

1.1 Group IV Photonics Based on Germanium

This thesis study demonstrates a nanosecond infrared laser-based crystallization process of germanium by implementing suitable laser parameters and deposition techniques to fabricate thin-film devices. Understanding the dynamics of the laser crystallization process of germanium thin-films by nanosecond pulsed infrared (IR) lasers is important for producing homogeneous, crack-free crystalline device-grade films for use in thin-film transistors, photo-detectors, particle detectors, and photovoltaic applications. Electron-beam-evaporation-deposited and physical vapor deposited amorphous germanium on glass substrates were subject to successive nanosecond laser pulses with a line focus. The laser crystallization of amorphous germanium thin-films results in micrometers via nanosecond pulsed IR laser.

Group IV photonics semiconductors (Germanium (Ge) and Silicon (Si)) are used in optoelectronics devices. In recent years, Group IV photonics semiconductors plays a great role in the near and mid-IR wavelength ranges due to offering strong nonlinearities in the bulk materials, high index contrast complementary-metal-oxide-semiconductor (CMOS) compatibility, and cost-effectiveness [2], [3].

Si has a several property which are the causes of the promising material in the devices. Firstly, Si has the higher band-gap energy (E_g=1.12 eV) in compare to Ge (E_g=0.67 eV) which allows the operation temperature several hundred degrees higher than for Ge [4]. Secondly, the high chemical stability of silicon dioxide which

promises semiconductor technology. Ge has higher electron mobility than Si; therefore, Ge is promising material in photovoltaic applications [5]. Besides, the low optical band-gap of Ge thin-films is suitable for its uses as IR-sensitive material.

Ge thin-films were investigated in the 1970s as typical of amorphous semiconductors [6]. In recent years, Ge has been used in IR detectors [7], solar cells [8], and optoelectronic devices [9], [10] since the direct band-gap energy of Ge is closer to the indirect transition energy than that of Si.

Si and Ge have an important differences about their band structures. The energy is plotted as a function of the wave vector k in Figure 1.1. Since the band diagram related to the direction within the crystal, the wave vector k along the main crystallographic directions <100> or <111> [10]. According to the energy-band diagram, the conduction band minimum and the valence band maximum occur at the same value for the k; therefore, the energy band gap is called direct. Other case, the maximum of the valence band and the minimum of the conduction band in Si and ge do not have the same wave vector, so the band gap is called indirect. Figure 1.1 shows the Ge has a lower indirect band gap of 0.67 eV and a very close direct transition of only $E_{\Gamma 1}$=0.8 eV. These properties determine the optical properties of Ge.

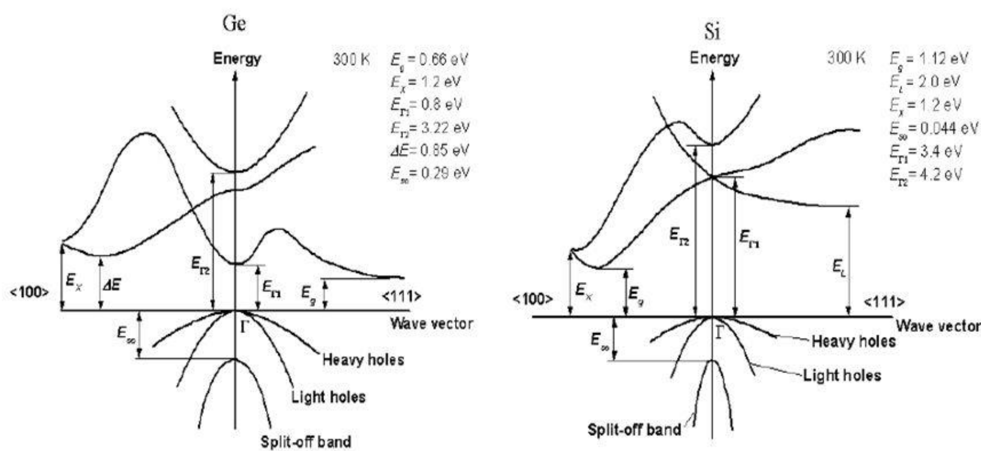

Figure 1.1 Band structure of Ge and Si [11].

Si and Ge are indirect; however, their absorption coefficient are different. Figure 1.2 shows that the Ge has a low absorption for photons with energy in the range of the 1850 nm. Absorption for photons increase with values wavelength below 1550 nm.

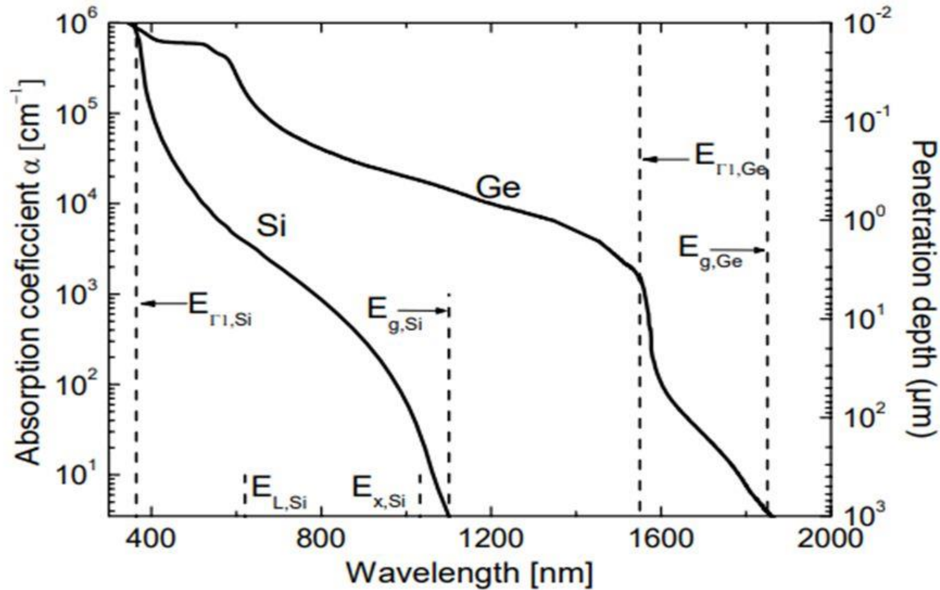

Figure 1.2 Absorption coefficient vs wavelength graph for Si and Ge [12].

1.2 Conventional Annealing Methods for Crystallization of Amorphous Germanium

Crystalline semiconductors outperform amorphous semiconductors in photovoltaic applications and optoelectronic sensor industry due to the superior electrical and optical properties compared to their amorphous counterparts.

Forming highly cyrstallized semiconductor thin-films on carrier substrates helps to improve the low efficiencies of low-cost amorphous semiconductors used in thin-film solar cells [13]. Amorphous Si thin-films have been studied using thermal and light-based crystallization for application in solar cells in order to benefit from the low cost of the film deposition versus the high cost of crystal growth while maintaining the crystalline quality of the active material [14]–[18]. In similar manner

to Si, high-quality crystallization of substrate-deposited a-Ge thin-films has attracted interest for its uses as an IR-sensitive material.

Different techniques have been applied to produce polycrystalline Ge (pc-Ge) films, such as solid phase crystallization (SPC) [19], metal-induced crystallization (MIC) [20]. However, crystallization of a-Ge with the SPC process requires a high annealing temperature of around 500 ºC, which is not applicable for every type of substrate. Besides, MIC has low-temperature processing but the employed semiconductors properties are deteriorated due to metal contamination.

1.3 Laser Crystallization of Amorphous Germanium Thin-Films

Laser annealing methods has been studied to achieve polycrystalline Ge thin-films [21]–[25] . Many types of laser such as continuous wave (CW) [21], [24], excimer [25] and femtosecond pulsed lasers [22] have been used to obtain high-quality crystalline thin-films. Unlike all the prior techniques, pulsed laser processing offers versatile control on the transition from the amorphous to crystal phase in short durations [23]. Besides, energy deposition can be controlled by using the scan speed and laser fluence in the pulsed laser irradiation system compare to CW laser irradiation [26]. The value of the output power is chosen to be in the kilowatt range in the CW laser system. In pulsed laser system, target heat accumulation on the surface can be achieved without an excessive thermal overshoot.

The laser crystallization (LC) process has a several advantages. One of the advantages of the LC is that the rapid cooling can be adjusted by changing the overlap ratio of the successive laser pulses. The other advantage of the LC of amorphous semiconductors that it provides the fabrication of crystalline thin-films on the glass substrate since the heating of the film is localized both spatially and temporally [27]–[29].

In light of recent developments reported in the literature (Table 1.1), the achieved crystallite in our study is prominently above the reported values.

Table 1.1 Achievements in the Literature

Laser Wavelength	Thickness of the Ge film	Deposition Technique	Substrate	Grain Size
nanosecond laser (532 nm) [30]	nc-Ge (100 nm)	inductively coupled plasma chemical vapor deposition	500 nm SiO_2	44-125 nm
pulsed Nd:YAG laser (1064 nm) [31]	100 nm to 1.4 µm	plasma enhanced chemical vapor deposition	silicon (001)	~ 400 nm
CW (532 nm) [32]	100 nm	molecular beam deposition	quartz glass	1-6 µm
CW (532 nm) [33]	100 nm	molecular beam deposition	quartz glass	~ 1-3 µm
femtosecond pulsed laser [22]	375 nm	plasma enhanced chemical vapor deposition	double side polished silicon wafers	20-80 nm
pulsed Nd:YAG [21]	500 nm	inductively coupled plasma chemical vapor deposition	quartz	1 µm

CHAPTER 2

THEORETICAL BACKGROUND

This chapter begins with a brief introduction of the dynamics of crystal growth of amorphous Ge thin-films. Following that, laser induced phase transformation of Ge, explosive crystallization of a-Ge thin-films and Raman scattering are desribed.

2.1 Dynamics of Crystal Growth of Amorphous Germanium Thin-Films

The state of amorphous material is a metastable. Compared to the crystalline state of a material, amorphous state of a materials have only short range order in their structures. That is the nearest neighbours keep on average a homogeneous interatomic distance; however, the periodicity of their arrangement quickly disappears with increase of the number of atoms.

The phase transition of a-Ge atoms to crystalline occurs at the temperature of the melting point (T_{ma}) of a-Ge (1210 K). For a-Ge, quenching of the liquid Ge does not result in amorphous but in polycrystalline material.

a-Ge thin-films can be obtained by e-beam evaporation and RF sputtering techniques, in these techniques, the cooling rate is considered to be of the order of 10^{10}- 10^{12} K/s. In the fabrication of the a-Ge thin films, high cooling rates lead to a structure that allows the existence of the a-Ge but a phase transition to the lower free-energy crystalline state can be induced at temperatures $T<T_{ma}$. The fabrication techniques play an important role in properties of a-Ge thin-films [34].

Figure 2.1 shows the free energy of the a-Ge (black curve) and the c-Ge (red curve) which respect to temperature allowing crystallization in order to occur below the melting temperature of c-Ge. Supercooled liquid Ge can exist at the temperature

between the melting temperature of a-Ge (T_{ma}) and the melting temperature of the c-Ge (T_{mc}).

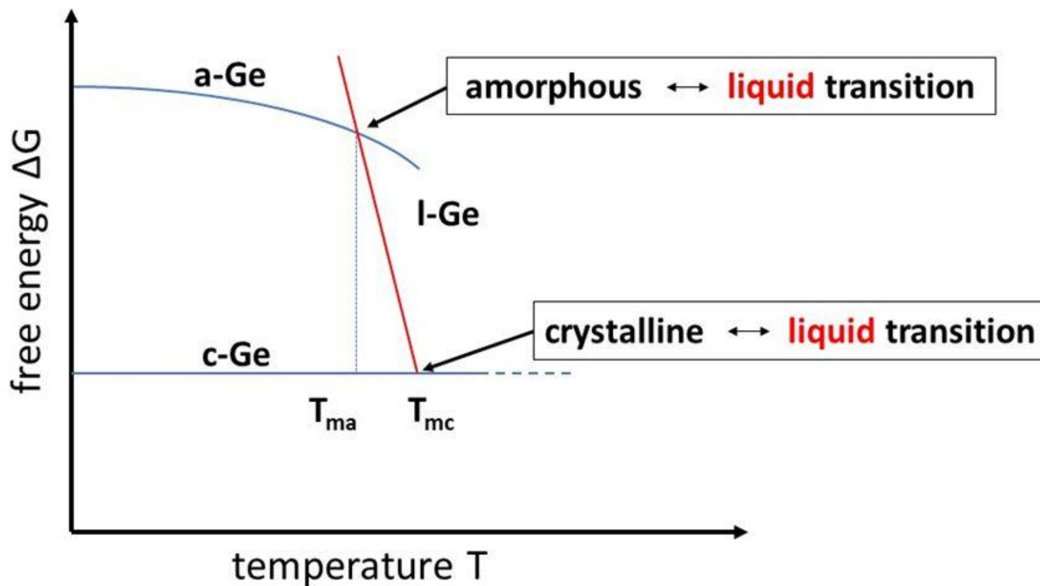

Figure 2.1 Free energy vs temperature graph of a-Ge and c-Ge [35].

The crystallization of Ge occurs by the release of the heat, and it is referred as explosive crystallization. Since the free energy of a-Ge is higher than the c-Ge and there is a way for a transition from a-Ge to c-Ge to occur below the T_{mc}, a-Ge state is a metastable at all temperatures compare to c-Ge [36]. This transition can be accomplished that the lower temperature for melting of a-Ge (T_{ma}) compared to the temperature of liquefaction of c-Ge (T_{mc}).

The supercooled liquid is called when the a-Ge is heated at temperature above the melting point of a-Ge but below the melting point for c-Ge ($T_{ma}<T<T_{mc}$). The range of this temperature, Ge presents a liquid-like properties although at a temperature below the temperature of the liquid at thermodynamic equilibrium [37]. The supercooled liquid state occurs in the time regime of nanosecond and picosecond. When the a-Ge is liquefied, the transition process can be occurred rapidly.

2.2 Laser Induced Phase Transformation of Germanium

When the laser beam interacts with the surface, some of the incoming laser beam reflects from the surface and some of the energy of the incoming laser beam passes to the material with the effect of absorption. The absorption interaction can be described as the interaction of the electromagnetic wave and the bound or free electrons of the material. Many different effects occur in the material after absorption such as heating (heat transfer), evaporation, plasma formation and melting. During material processing, the increase in temperature and the ionization of the vapor phase occur in the material as heating, evaporation, plasma formation and ablation. If the laser fluence is very high and the region where the laser beam interacts with the material can exceed the boiling temperature, evaporation and thermal stress occur [20], [38], [39]. This causes material removal, and this process is called thermal ablation. If the time between pulses is too short, the material remains around the ablation threshold. In this situation, a high repetition rate is required for an efficient ablation process. For an effective ablation process, laser energy is transferred. The area should be checked with beam quality and beam diameter.

The band gap energy of c-Ge is 0.67 eV which is close to the energy of the IR photons of a nanosecond pulsed IR laser at a wavelength of 1064 nm. The laser crystallization (LC) process helps to adjust the rapid cooling by changing the overlap ratio of the successive laser pulses. The LC process is initiated with the melting of the a-Ge thin films by absorption of IR irradiation via a nanosecond pulsed IR laser. The absorption of the irradiated laser beam in the Ge thin films initiates the generation of free carriers, then which subsequent linear absorption of light by valence electron follows, leading to non-radiative electron-hole pair recombination and transfer of the energy to the bulk atoms (a-Ge atoms) in the form of heat. The lifetime of non-radiative recombination is longer than that of a semiconducting interaction [40], [41]. Even if the non-radiative transition time is short, the absorbed energy by the free carriers is transferred in the form of heat.

When laser induced phase transformation is considered, the light-matter interaction and heating should be discussed in detail. The amount of light absorbed by a sample is related to the volume of the layer. The amount of energy of the light that is transferred and entered to the layer are result of the absorption of the light. If the material is optically homogeneous, Beer-Lambert Law is expressed as

$$I = I_s e^{(-\alpha d)} \tag{2.1}$$

where I is the intensity of the laser energy in a material, I_s is the energy of the laser on the surface, α is the optical absorption coefficient and d is the distance from the surface [42].

During the phase change induced by the melting, the heat conduction in solid and liquid phases is expressed as a differential equation.

$$\rho C_p \frac{\partial T}{\partial t} - \nabla(k \nabla T) = Q \tag{2.2}$$

where ρ is the mass density, C_p is the specific heat, T is the temperature, k is the thermal conductivity of the material and Q is the volumetric heat source [43]. The volumetric heat source can express with the phases of the material (substrate, amorphous, liquid and polycrystalline) and it is related to the absorption of the laser beam in the material. Using the Beer-Lambert Law, Q is also expressed as

$$Q = I\,(1 - R)\alpha e^{(-\alpha d)} \tag{2.3}$$

where R is the reflectivity, α is the absorption coefficient and d is the thickness of the sample.

The phase change effect for melting is expressed in the enthalpy method as

$$C_p(T) = C'_p(T) + g(T)L_m \tag{2.4}$$

where $C'_p(T)$ is the specific heat as a function of temperature, $g(T)$ is the Gaussian distribution function and L_m is the latent heat of fusion. The Gaussian distribution function $g(T)$ is defined as

$$g(T) = \frac{1}{\Delta T\sqrt{\pi}} \exp\left(-\left(\frac{(T-T_m)^2}{\Delta T^2}\right)\right) \tag{2.5}$$

ΔT is the temperature range corresponding to the phase transition and T_m is the melting point of a-Ge. The a-Ge is heated until the melting of the surface. Then, a liquid layer of Ge starts to solidify. Due to the releasing the latent heat and the rapid cooling, a-Ge layer starts to melt, and pc-Ge grains are formed.

When the laser fluence is very high and the region where the laser beam interacts with the material can exceed the boiling point, evaporation and thermal stress occur. This causes material removal, and this process is called thermal ablation. When the time between pulses is too short, the material remains around the ablation threshold. In this situation, a high repetition rate is required for an efficient ablation process.

2.3 Explosive Crystallization of Amorphous Germanium Thin-Films

Due to the excessive latent heat, increasing the temperature of a-Ge layer cause to liquify the Ge layer and this liquified layer propagates along the a-Ge regions. The phase transition propagates through the a-Ge regions and this process is called explosive crystallization (EC) [44].

When the laser crystallization (LC) of a-Ge is performed, EC occurs as an initiating effect on crystallization [40], [41], [45], [46]. The EC initiates with the melting of a-Ge. Below the T_{ma} of a-Ge (1210 K), there is no sign of crystallization [47], [48]. During the crystallization process, the free energy is released to sustain the crystallization on the surface and to locally heat up the substrate. The self-thermal enhancement induces a self-sustained crystallization leading to the formation of a liquid region and to surface damage eventually [37]. By the slow proceeding crystallization with a lower scan speed of the laser, these damages can be avoided. At a low scan speed of laser, slow releasing the latent heat can occur due to a thin-film thickness associated with a high energy loss in the substrate.

A nanosecond pulsed laser allows control of the energy flux and the thermal gradient formation. When the energy is delivered during the laser pulse heats a surface region of an a-Ge to T_{ma}, a liquid surface layer highly undercooled with respect to c-Ge originates [49].

2.4 Raman Scattering

Raman spectroscopy is a method in which scattered light is used to measure the vibrational energy modes of a surface or sample. When light hits the surface and is scattered by a molecule, the oscillating electromagnetic field of a photon stimulates a polarization of a molecular electron cloud. This leaves when the energy of the photon transferred is at a higher energy potential. The energy of the molecule does not change after its interaction with the photon and the wavelength of the scattered photon is same with the incident photon. This phenomenon is called an elastic or Rayleigh scattering. As seen in Fig. 2.2, Another scattering is called inelastic scattering process with the transferring the energy between the scattered photon and the molecule. When the molecule gains energy from the photon, the scattered photon loses energy, therefore, the wavelength of the scattered photon increases. This is called Stokes Raman scattering. In the opposite case, when the molecule loses energy by the relaxation of a lower vibrational level the scattered photon gains the energy; therefore, the wavelength of the scattered photon decreases which is called Anti-Stokes Raman scattering [50].

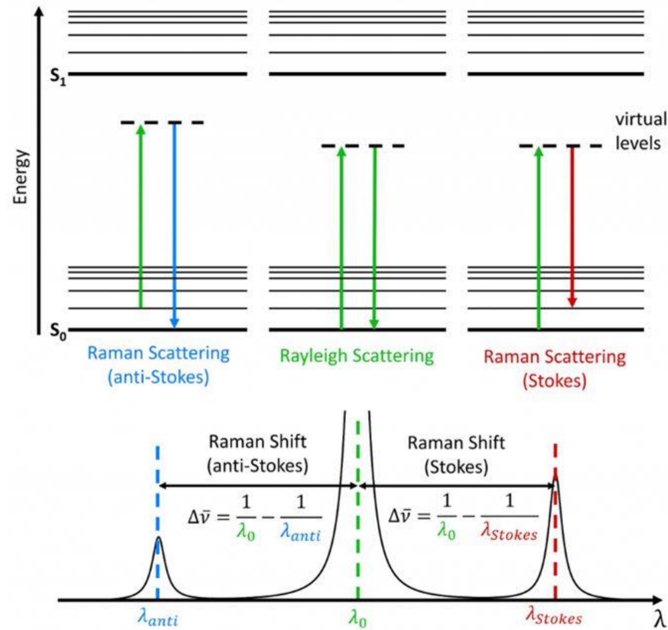

Figure 2.2 Anti-stokes, rayleigh and stokes scattering [51].

Raman spectroscopy measures the energy change between the scattered photons and the incident photons which are related with the Stokes and anti-Stokes Raman scattering. This is measured as the change in the wavenumber (cm^{-1}) from the incident light. Raman Spectroscopy measures the change in wavenumber. The Raman scattering position can be converted to a Raman shift away from excitation wavelength. To determine the Raman shift, the wavelengths of scattered and excitation light is used, and the following equation is defined as in Equation (2.6);

$$\Delta\nu(cm^{-1}) = (\frac{1}{\lambda_0(nm)} - \frac{1}{\lambda_1(nm)}) \times \frac{(10^7 nm)}{(cm)} \tag{2.6}$$

where $\Delta\nu$ is the Raman shift in cm^{-1}, λ_0 is the wavelength of the excitation light in nm, and λ_1 is the wavelength of the scattering light from the sample in nm.

2.5 Raman-Strain Relations in Strained Germanium

For semiconductor materials, the residual and mechanical stress are important when designing a device [52]. Mechanical stress occurs between the thin-film and the substrate [53]. The lattice mismatch at the interfaces of different materials or semiconductors, thermal mismatch because of the different coefficients of thermal expansion of the materials and internal stress of the different materials or semiconductors layers grown on the substrate can be causes of biaxial and uniaxial stress inside the materials. Stress can induce the formation of cracks at the locations which has a high local stress [54]–[56]. The Raman spectra of the crystalline materials depends on the phonon band structure of the lattice of the materials [57], [58]. The mechanical strain and stress cause to changing the phonon frequencies. As pointed out by centres of the Raman peak, the displacement of atom varies the phonon frequencies [55], [59].

Ge is a promising material for monolithic light sources. When the high value of strain is applied to Ge, the light emission properties of Ge improve, and Ge becomes a direct band gap semiconductor.

The ratio between the values of strain along the different directions/orientations is called the strain ratio. The strain ratios depend on the nature of the stress such as biaxial and uniaxial. The uniaxial stress (100), the uniaxial stress (110) and the bi-axial stress (001) are expressed following [60].

$$A: \frac{\varepsilon_{010}}{\varepsilon_{100}} = \frac{\varepsilon_{001}}{\varepsilon_{100}} = \frac{S_{12}}{S_{11}} \tag{2.7}$$

$$B: \frac{\varepsilon_{001}}{\varepsilon_{110}} = \frac{2 \times S_{12}}{S_{11} + S_{12} + S_{44}/2} \tag{2.8}$$

$$C: \frac{\varepsilon_{010}}{\varepsilon_{001}} = \frac{\varepsilon_{100}}{\varepsilon_{001}} \frac{S_{11} + S_{12}}{2 \times S_{12}} \tag{2.9}$$

The strain components ε_i relates to the longitudinal strain along the axis i. Moreover, the three possible Raman frequencies are represented as a function of the phonon

deformation potentials (p, q and r) and the elastic coefficients (S_{11}, S_{12} and S_{44}). The corresponding equations of (100) uniaxial stress, (110) uniaxial stress, (001) biaxial stress and (111) uniaxial stress are expressed as

$$A: \Delta\omega_1 = \Delta\omega_2 = \Delta\omega_{TO} = \frac{pS_{11}+2qS_{12}}{2S_{11}\omega_0}\varepsilon_{100}\ ; \tag{2.10}$$

$$\Delta\omega_3 = \Delta\omega_{LO} = \frac{pS_{12}+q(S_{11}+S_{12})}{2S_{11}\omega_0}\varepsilon_{100}, \tag{2.11}$$

$$B: \Delta\omega_{1,2} = \Delta\omega_{TO} = \frac{p(S_{11}+S_{12})+q(S_{11}+3S_{12})\pm rS_{44}}{2\omega_0(S_{11}+S_{12}+\frac{S_{44}}{2})}\varepsilon_{110}; \tag{2.12}$$

$$\Delta\omega_3 = \Delta\omega_{LO} = \frac{pS_{12}+q(S_{11}+3S_{12})}{\omega_0(S_{11}+S_{12}+\frac{S_{44}}{2})}\varepsilon_{110}, \tag{2.13}$$

$$C: \Delta\omega_1 = \Delta\omega_2 = \Delta\omega_{TO} = \frac{1}{2\omega_0}\left(p + q\,\frac{S_{11}+3S_{12}}{S_{11}+S_{12}}\right)\varepsilon_{100}; \tag{2.14}$$

$$\Delta\omega_3 = \Delta\omega_{LO} = \frac{pS_{12}+q(S_{11}+S_{12})}{\omega_0(S_{11}+S_{12})}\varepsilon_{100}, \tag{2.15}$$

$$D: \Delta\omega_1 = \Delta\omega_2 = \Delta\omega_{TO} = \frac{(p+2q)(S_{11}+2S_{12})+2rS_{44}}{2\omega_0(S_{11}+2S_{12}+S_{44})}\varepsilon_{111}; \tag{2.16}$$

$$\Delta\omega_3 = \Delta\omega_{LO} = \frac{(p+2q)(S_{11}+2S_{12})-rS_{44}}{2\omega_0(S_{11}+2S_{12}+S_{44})}\varepsilon_{111}, \tag{2.17}$$

The Raman shift-strain relationship in Ge is linear, formulated as follows

$$\Delta w = k \times \varepsilon \tag{2.18}$$

where Δw is the shift in the Raman peak position of pc-Ge with respect to the reference Raman peak position of bulk c-Ge in units of cm^{-1}, k is the corresponding linear coefficient and ε is the tensile stress in units of GPa. The sign of k changes with the type of stress on Ge film. Tensile stress on the Ge film has a positive value whereas compressive stress has a negative value [42], [43]. Gassenq *et al*. have compared to the transverse optical (TO) linear coefficients (k_{TO}) with the literature [42]. In the case of quasi-backscattering Raman scattering, the longitudinal optical (LO) phonons are active only for the crystal orientation (001), while for crystals oriented (110), the TO phonons are active, and for crystals oriented (111), both types of phonons are active.

Local heating leads to red-shift of phonon frequencies due to anharmonism. It would be possible to estimate the size of germanium nanocrystals also from the increase in the width of the peaks, as in well-known improved phonon confinement model for analysis of Raman spectra of germanium nanocrystals. Estimating the size of the crystals is not applicable to the crystallite size in the order of tens of micrometres. The size of nanocrystals, which were discussed in Volodin *et al*. [61]–[63] are in the order of tens of nanometres. The phonon confinement model is mostly adequate for the crystalline size below 20 nm [61], [64]. The effects of the local heating, which causes the red-shift, is dominant at the size of around 5 nm crystallites, whereas the dominant cause of the red-shift is caused by the tensile stress. It is worth mentioning that the results of calculations in the improved phonon confinement model are correct for a broad range of Ge NCs sizes from about 1.3 to 10 nm [63]. The red-shifts in the Raman spectra of germanium nanocrystals were studied by Maeda *et al*., whereas the dominant factor causing the red-shift of Raman peaks is attributed to the tensile stress on the film between the grains at the micrometre scale in the recent studies as well [65], [66].

When the distribution density of Ge crystal domains is considered, the density of crystalline materials is somewhat higher than the density of amorphous materials and crystallization can induce some stretching of the crystals [67]. The crystallites, whose dimensions are larger than 100 nm, can consist of slightly misoriented

nanocrystals, contain structural defects, or experience stretching strains [53], [62], [68], [69].

In this thesis study, the thickness of the Ge films is thicker than that of the Ge films used in the study of Hao *et al* [70]. The Ge film of 15 nm thick is semi-transparent at the wavelength of 512 nm, it transmits ≈28% and reflects ≈41% of the incident light. The dependence of Raman scattering cross section ratios of nanocrystalline Ge to amorphous Ge on sizes of 300 nm is not applicable in Raman spectroscopy setup. It was reported that ~200 nm thick Ge films exhibit almost no transmission below the wavelength of 600nm which is not practical to apply the Raman scattering cross section analysis [62]. The only circumstance in which this ratio can be approximated is by using intense excitation light for the Raman analysis. There will be a trade-off due to the local phonon confinement caused by local heating [71]. This local heating most probably starts to dominate the shifts of Raman peaks.

.

CHAPTER 3

IMPROVEMENT OF THE LINE FOCUS SCANNING OPTICS

In this chapter, constructing of a line focus scanning system and describing the Gaussian and flat-top beam profile by the cylindrical lens and the Powell lens is given, respectively.

3.1 Introducing of Laser Marking System

Laser parameters such as pulse energy, repetition rate, scan speed and pulse duration play an important role in crystallization of semiconductors. When pulse energy increases, the depth of the processed region also increases. The pulse energy depends on the average output power and repetition rate. Furthermore, the laser fluence depends on the output power and effective focal spot size.

FiberLast Flast-NanoMARK 20W marking laser system is used in this study. This laser is diode pumped MOPA laser with Ytterbium ion (Yb3+) doped fiber amplifiers. A nanosecond pulsed IR laser with a pulse duration of 200 ns, a repetition rate of 100 kHz at the wavelength of 1064 nm was used. The maximum average power is 20W. The laser beam was focused on the film surface by a telecentric lens after passing through a 2-D galvo-mirror set at a distance of 163 mm.

3.2 Gaussian Beam Profile by the Cylindrical Lens

An additional cylindrical lens is utilized to expand the spot focus into a line focus in Figure 3.1. The cylindrical lens is 20 mm long and has a 10 mm focal length, where it focuses the beam in a high-aspect elliptical shape with dimensions of 45 × 1250 µm. The beam profile is flat-top Gaussian in the long axis, and fluence is homogeneous over the pulse cross-section. According to ray optics, scan step size

lines (distance between the center of ellipses) are 1 mm. The curved surface of the cylindrical lens faces the incoming laser beam from the f-theta lens in order to avoid optical abberations.

The cylindrical lens is integrated with an kinematic rectangular optics mount in between the f-theta lens and the target surface. Since the length of the cylindrical lens is 20 mm and the aberations caused by the incident angle on the cylindrical lens, the maximum line length of scanning with a cylindrical lens is 18 mm.

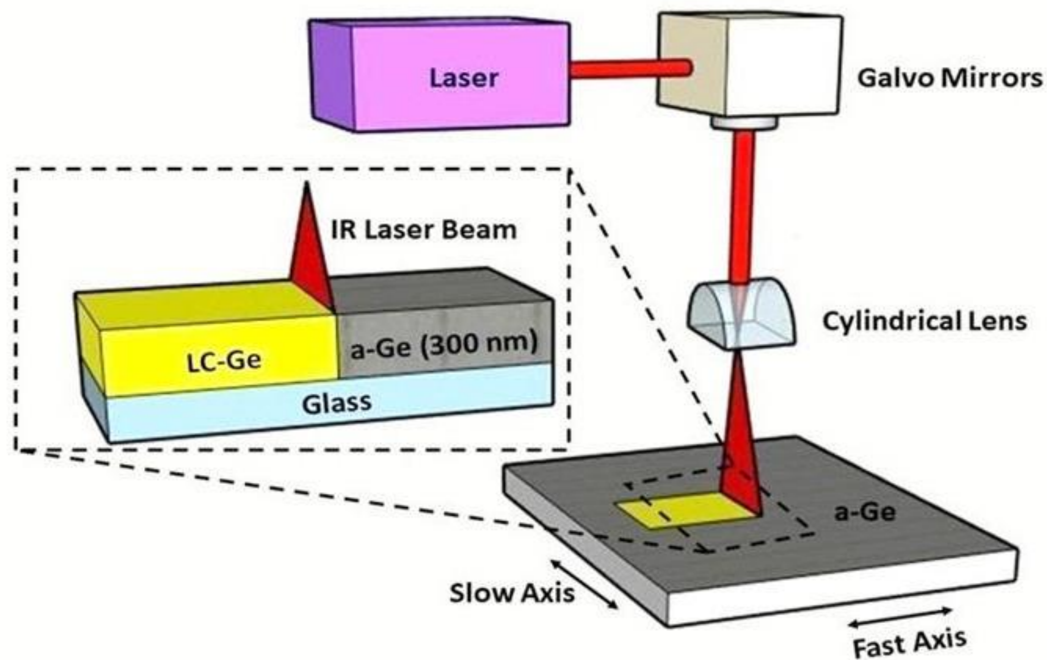

Figure 3.1 Laser marking system with a cylindrical lens.

3.3 Flat-Top Beam Profile by the Powell Lens

The Powell lens is a line generator which looks like a round prism with a curved roof line. And the Powell lens can strech a narrow incident laser beam into a straight line uniformly. The range of the fan agnle vary from 1º to 120º. The width of the Powell lens fan angle depends on the refractive index of the glass and the roof angle. The higher refractive index of the glass and the steeper the roof cause to the wider the fan

angle, then the projected distance will be longer line. In this study, the apex length of 6.30 mm lens is used with a fan angle of 30 º.

The comparision between the cylindrical lens and the Powell lens is shown in Figure 3.2. Compared to the cylindrical lens, the Powell lens generates a laser profile with more uniform energy distribution. For achieving a wider scanning area, only an increase in the average power equal to the increase in the focal line length will be sufficient.

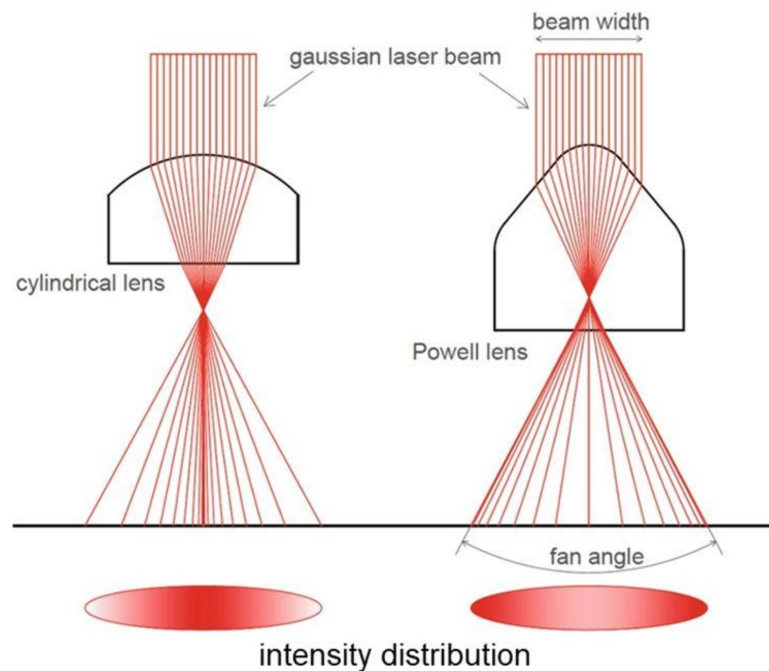

Figure 3.2 Beam profile of the cylindrical lens and the Powell lens [72].

The line focus scanning system is adapted to form a flat-top line shaped focus on the surface of germanium thin-films. The laser beam was focused on the film surface by a telecentric lens after passing through a 2-D galvo-mirror set at a distance of 182 mm [73]. Figure 3.3 shows that the laser beam comes across the galvo (scanning) mirror, and it is reflected to the telenctric F-theta (F_θ) lens. The F_θ lens helps the

laser beam to focus perpendicular on material surface. When the galvo mirror moves, the laser beam is perpendicular to the surface the whole scanning time.

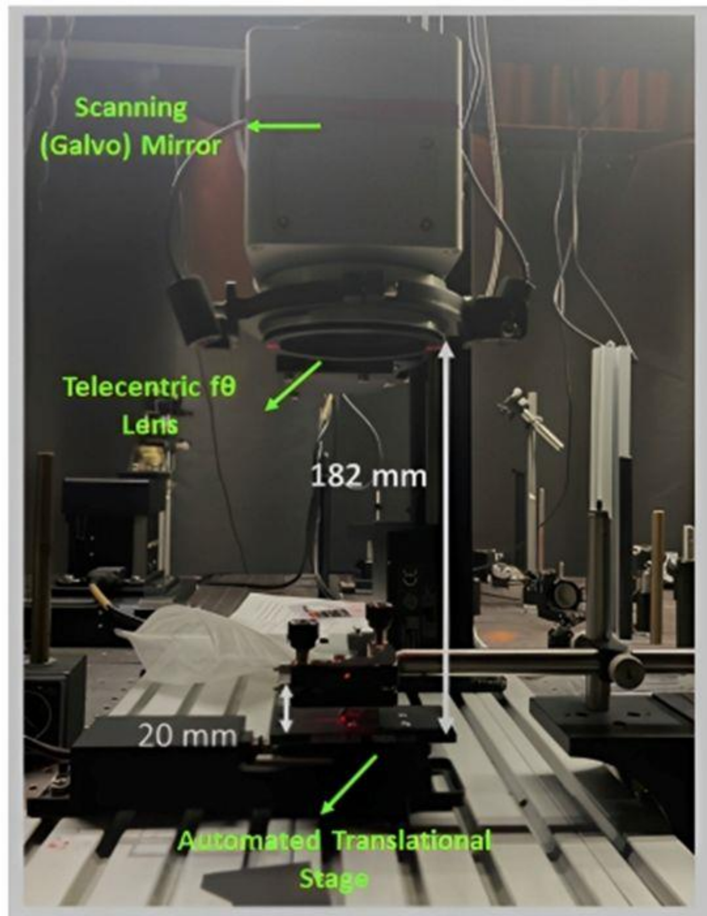

Figure 3.3 A schematic view of the laser system with a Powell lens.

The optimized stretching length and apex diameter vs working distance graph is shown in Figure 3.4. According to this graph, the stretching length of 3 mm is sufficient to achieve successive laser fluences for melting of a-Ge.

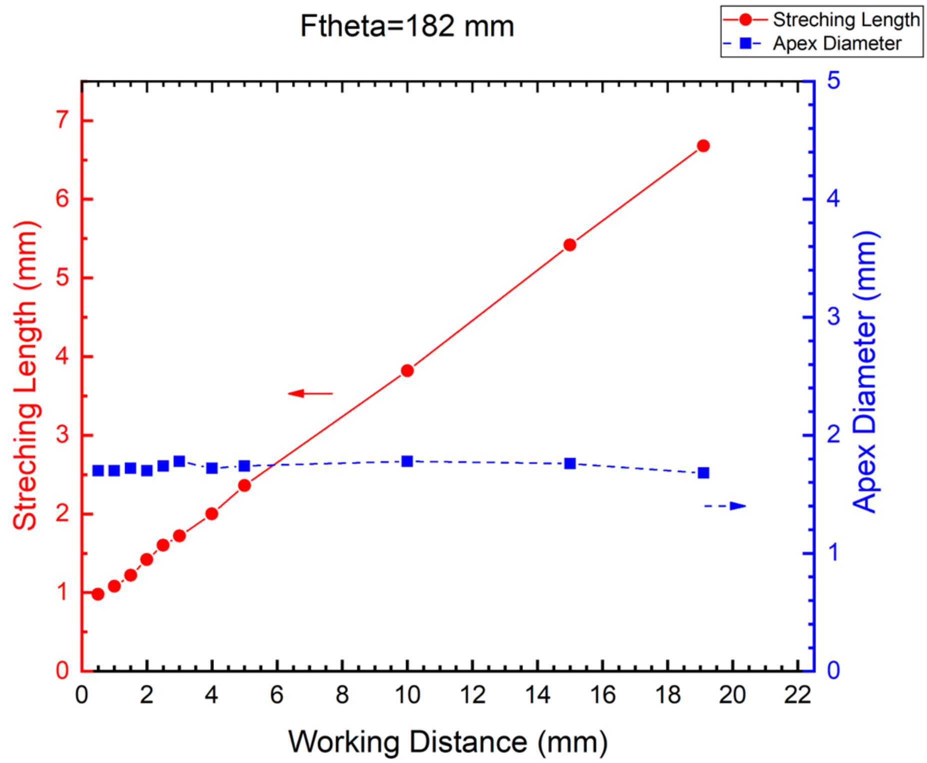

Figure 3.4 The streching length and apex diameter vs working distance graph.

CHAPTER 4

LASER CRYSTALLIZATION AND CHARACTERIZATION OF AMORPHOUS GERMANIUM THIN-FILMS DEPOSITED BY E-BEAM

300 nm thick a-Ge thin films on glass substrate are prepared by an electron-beam evaporator. In this chapter, the processed LC-Ge thin-films are characterized using Raman spectroscopy, optical microscopy and EBSD.

4.1 Preparation of a-Ge Thin-Films

a-Ge with a thickness of 300 nm is deposited on 1.1 mm thick solar glass substrates at room temperature using an e-beam evaporator at a rate of 3.0 A/s using 5N Ge as a source. The glass substrates are cleaned by a series of ultrasonic cleaning process (acetone, isopropanol, and DI water, 10 min each). The thickness and deposition rate are monitored with a quartz oscillator.

4.2 Laser Crystallization of a-Ge Thin-Films and Line Focus Scanning by the Cylindrical Lens

All LC process of a-Ge thin-films was studied by a nanosecond pulsed laser at room temperature in air. A nanosecond pulsed IR laser with a repetition rate of 100 kHz and a pulse duration of 200 ns at a wavelength of 1064 nm. The laser beam was focused on the film surface by a telecentric lens after passing through a 2-D galvo-mirror set at a distance of 163 mm. An additional cylindrical lens is utilized to expand the spot focus into a line focus. The cylindrical lens is 200 mm long and has a 10 mm focal length, where it focuses the beam in a high-aspect elliptical shape with dimensions of 45 × 1250 µm. The distance between the center of ellipses are 1 mm. The beam profile is flat-top Gaussian in the long axis, and the laser fluence is homogeneous over the pulse cross-section. The beam profile becomes a flat-top

Gaussian in the long axis, whereas the profile along the short axis maintains its usual Gaussian profile.

4.2.1 LC-Processed Regions with Non-Overlapping Pulses

When semiconductors processed with a pulsed laser, controlling the overlapping of pulses is important to achieve high quality crystallites. The value of scan speed is varied to control the overlapping factor (O_f) of successive laser pulses.

$$O_f = (1 - \frac{V_S/f}{D_S + V_S\tau}) \quad (4.1)$$

In the formula above, O_f is calculated with D_s, V_s, f and τ refer to the length of the focus along the scan direction, scan speed, the repetition rate of the laser pulses and the pulse duration of the laser, respectively [74].

4.2.1.1 Optical Microscope Images

Under the optical microscope, the crystallites can be seen easily due to the phase contrast. The optical microscope images of LC-processed regions with laser fluences of 272 and 416 mJ/cm^2 at a fixed overlapping factor of 99.9% (scan speed of 4600 mm/s) in Figure 4.1.

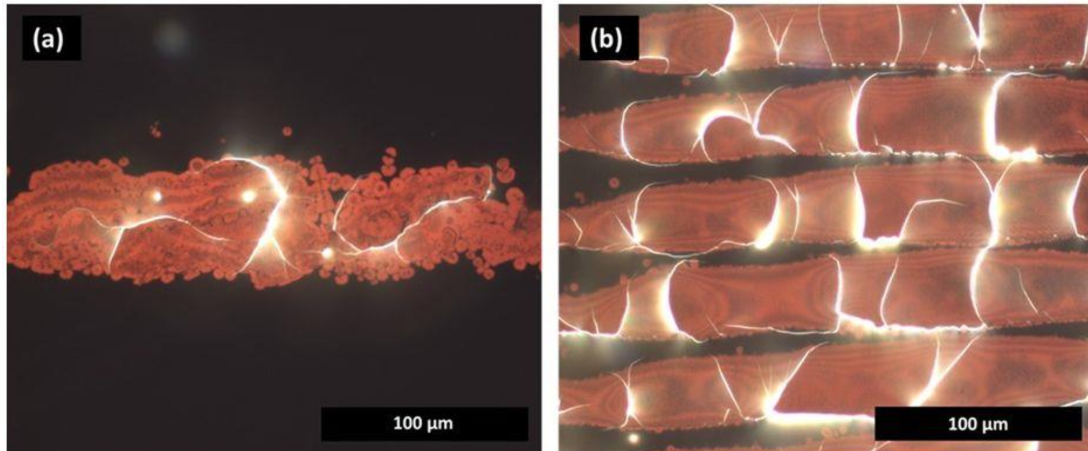

Figure 4.1 Optical microscope images of LC-processed regions with laser fluences of (a) 272 and (b) 416 mJ/cm^2 at a fixed scan speed of 4600 mm/s (non-overlapping pulses).

The laser fluence of a single laser pulse is 272 mJ/cm^2 for the crystallization threshold. The crystal domains grow imperfectly with cracks.

4.2.1.2 Raman Analysis

All LC regions are checked by Raman spectroscopy to confirm their crystallinity. Figure 4.2 shows the Raman analysis of LC-Ge with different laser fluences at a fixed scan speed 4600 mm/s (non-overlapping pulses). From laser fluences of crystallization threshold and damage threshold, the FWHM gets broader. The wider linewidths may be due to lower melting and cooling durations [60], [75].

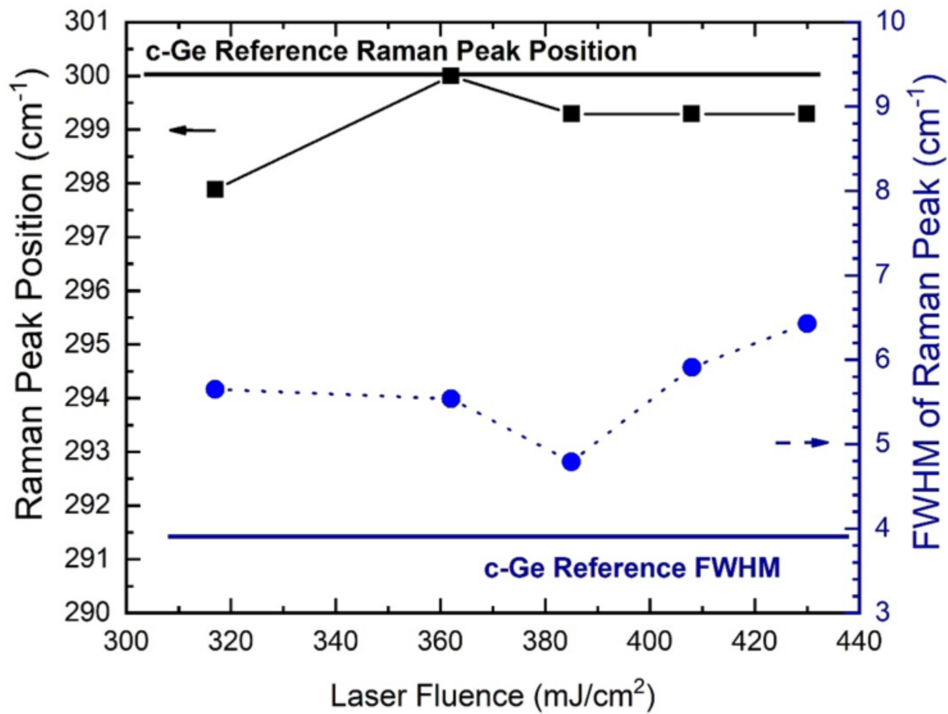

Figure 4.2 Raman analysis of LC processes regions with different laser fluences at a fixed scan speed of 4600 mm/s (non-overlapping pulses).

The overlapping factor of laser pulses and the laser fluence plays an important role in achieving the high-quality pc-Ge films. To initiate the crystallization phenomena, the value of laser fluence for non-overlapping pulses is higher than the value of laser fluence for overlapping pulses. The reason of that, the overlapping laser pulses increase the sufficient heat energy to initiate the melting of the Ge film. Below the laser fluences of 272 mJ/cm^2 with a scan speed of 4600 mm/s does not provide sufficient energy for the melting of Ge film.

4.2.2 LC-Processed Regions with Highly Overlapping Pulses

After the laser fluence optimization at a scan speed of 5 mm/s, the effect of the scan speed on the LC processes of the Ge films keeping the laser fluence constant at 110 mJ/cm^2 is investigated.

4.2.2.1 Optical Microscope and SEM Images

The optimization of the laser fluence plays a crucial role in achieving high-quality pc-Ge film. When the energy of crystallization threshold of the film is close to the laser fluence, the laser crystallization starts. Firstly, 300 nm a-Ge layer thickness on glass substate is deposited using e-beam evaporator.

Figure 4.3 shows the optical microscope images of the LC of a-Ge at a fixed scan speed 5 mm/s with laser fluences of 45, 68 and 110 110 mJ/cm^2, respectively. The crystalline domains can easily be observed under an optical microscope with phase contrast. According to optical microscope image, the laser crystallization begins with laser fluences of 45 mJ/cm^2.

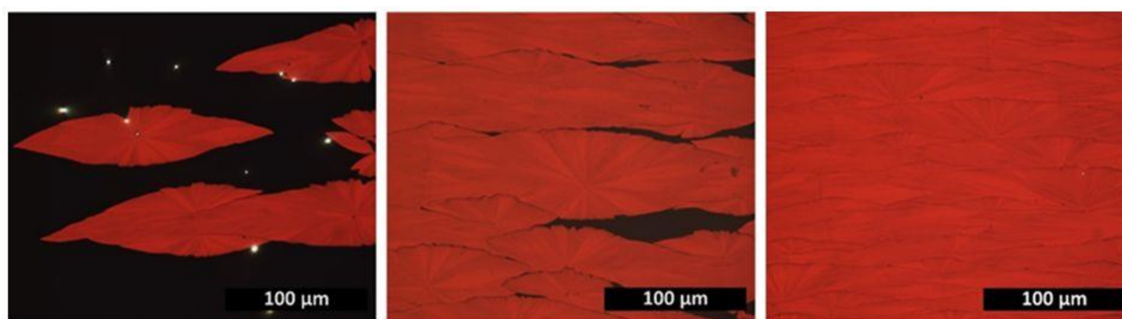

Figure 4.3 Optical microscope images of LC of a-Ge with a laser fluences of 45, 68, 110 mJ/cm^2, respectively.

The effective laser fluence and scan speed are fixed at the value of 110 mJ/cm^2 and 5 mm/s, respectively. In Figure 4.4, LC-processed regions with laser fluences of 115 and 110 mJ/cm^2 are analysed with SEM.

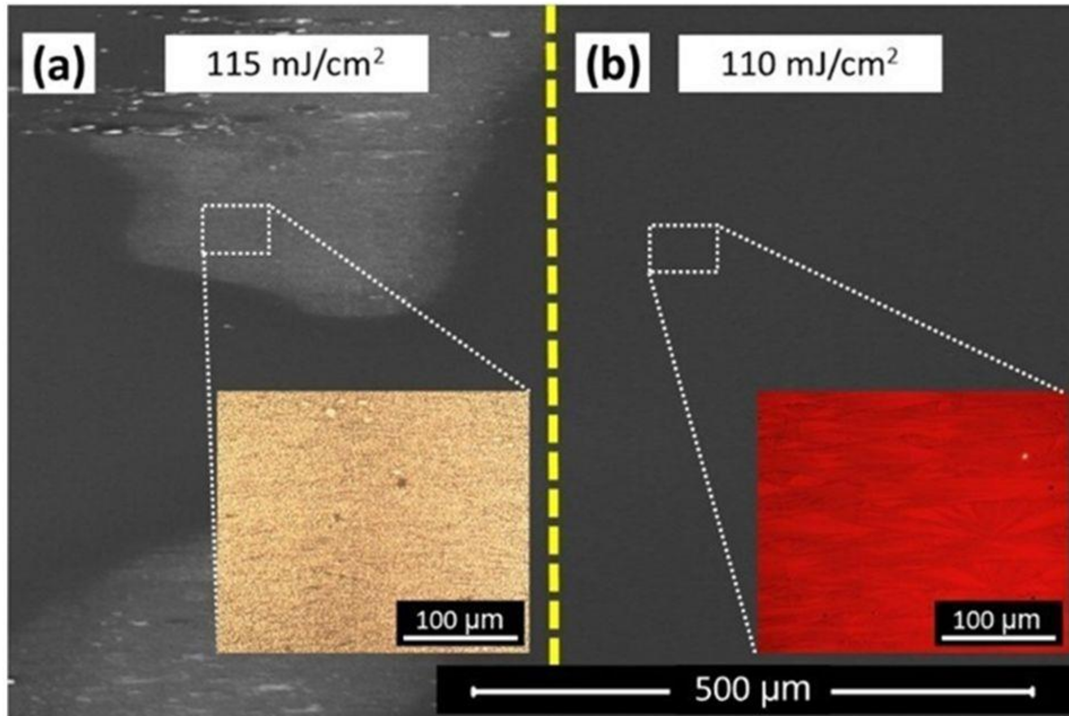

Figure 4.4 SEM images of the LC-processed regions with laser fluences of (a) 115 mJ/cm^2 and (b) 110 mJ/cm^2 with corresponding optical microscopy images in the insets.

Figure 4.4 (a) exhibits the structural deformation in the form of large creaters and defective formations. The sample processed with laser fluences of 110 mJ/cm^2 shows homogenous and smooth surface morphologies after the laser crystallization in Figure 4.4 (b). Ge crystallite domains extends radially, and they are centred around defects during melting (liquefaction) in Figure 4.4 (a). Ge has a high energy density in a liquid phase [76]. Therefore, defects in the molten area act like seeds, which leads to the crystallization of liquid Ge starting from the defect and growing radially outward during cooling in Figure 4.4 (b).

4.2.2.2 Raman and Tensile Stress Analysis

Figure 4.5 summarizes the Raman spectroscopy analysis of LC-Ge performed at different laser fluences with a fixed scan speed of 5 mm/s.

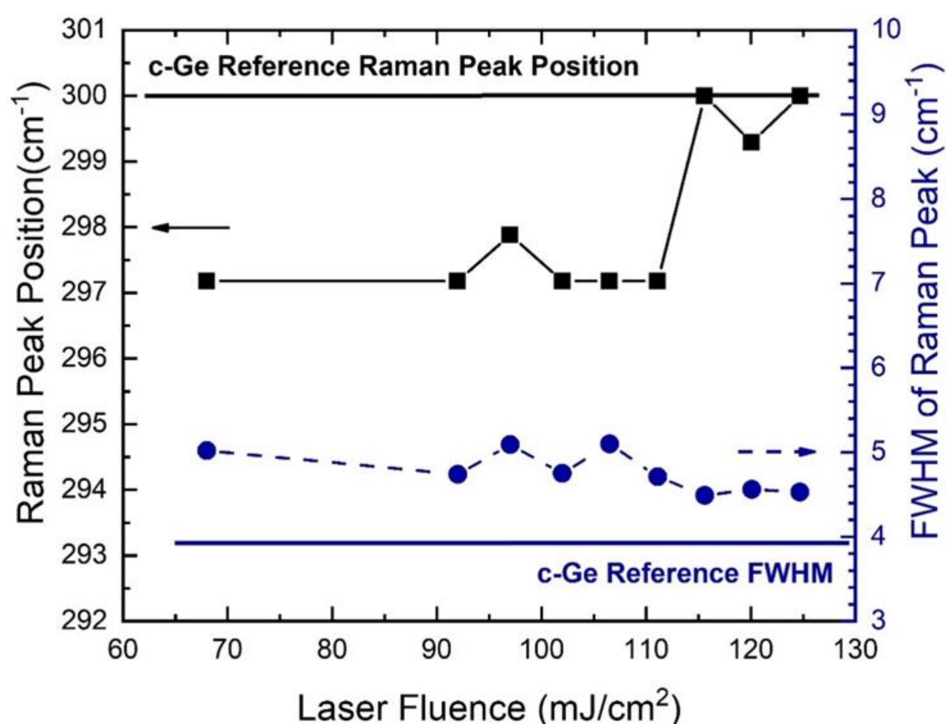

Figure 4.5 Raman peak position and FWHM of the LC-Ge thin films as a function of the laser fluence with the scan speed of 5 mm/s.

The entire Raman spectroscopy analysis are conducted in a backscattering geometry; thus, only the singlet transverse optical phonon (TO) is detected. The Raman shift was calibrated using the TO line (300 cm^{-1}) of single-crystal Ge (100). The excitation wavelength of a 532 nm diode-pumped solid-state laser with a measured power of 300 µW and 33 µm spot diameter is incident on the LC films through a microscope where the light is focused and collected by an objective lens and sent fiber-optically to a Raman spectrometer (Horiba-JobinYvon iHR550) at the setting of 1800 g/mm grating. By considering the reference c-Ge (Ge-GE, TO) peak position at 300 cm^{-1} with the full width at half-maximum (FWHM) of 3.88 cm^{-1}, the sample processed at a laser fluence of 110 mJ/cm^2 gives a Raman peak positioned at 297 cm^{-1} with FWHM of 5.6 cm^{-1}, which indicates a relatively good crystal quality of the LC film. Laser fluences above 110 mJ/cm^2, the linewidth of the Raman band gets larger because of the high concentration of defects or reduced crystallite size [77]. This shift in the Raman peak of LC-Ge from that of reference c-Ge is attributed to a tensile stress build-up in the film occurring during the formation of crystallites. Increasing

the laser fluence leads to an increase in the size and number of crystallites, which causes the stress to build up further due to thermal mismatch between these crystallites and the substrate or each other.

The various scan speeds at a fixed laser fluence are studied to examine the effects of overlapping laser pulses. Figure 4.6 summarizes the Raman analysis of LC-Ge at scan speeds between 5 and 30 mm/s at a fixed laser fluence of 110 mJ/cm^2. According to the optical microscope and Raman spectroscopy, there is no sign of the crystallization at scan speeds above 35 mm/s. The scan speed of 5 mm/s gives a Raman peak position at 297 cm^{-1} with an FWHM of 5.6 cm^{-1}. The peak position and FWHM depend on the abundance of defects, average crystallite size and stress [75].

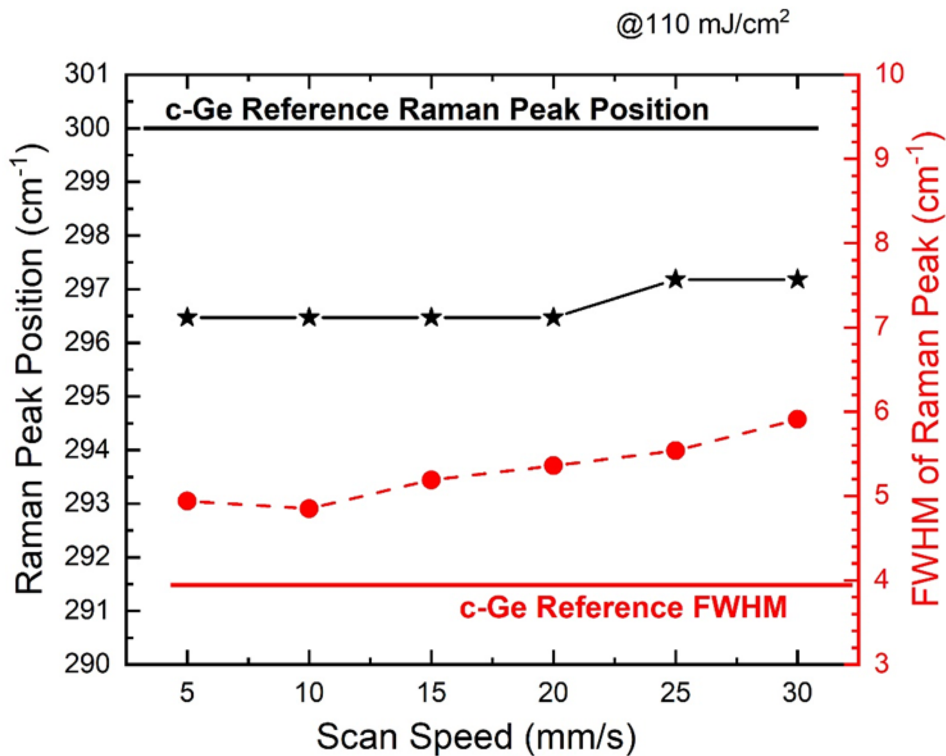

Figure 4.6 Raman peak position and FWHM of the LC-Ge thin films as a function of scan speed at a laser fluence of 110 mJ/cm^2.

In Fig. 4.7 shows the comparison of Raman spectra of a-Ge, LC-Ge and bulk c-Ge. The bulk c-Ge Raman peak is positioned at 300 cm^{-1} with a peak width (FWHM) of

~4 cm^{-1}. The LC-Ge film exhibits a Raman peak positioned at 296 cm^{-1} with a peak width of 5.6 cm^{-1}. The linewidth of LC-Ge is broader than that of bulk c-Ge due to tensile stress occurring on the surface of the film. This shift of the Raman peak position to lower wavenumbers with a larger FWHM compared to that of bulk c-Ge implies that LC-Ge is subject to tensile stress.

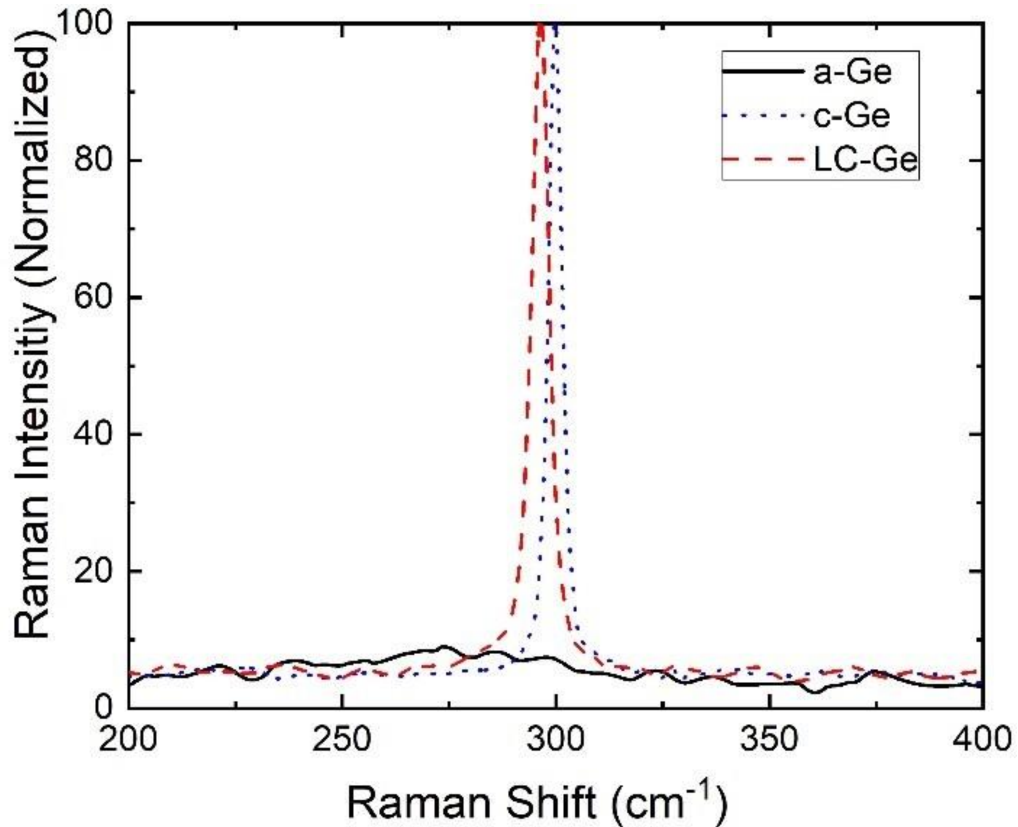

Figure 4.7 Raman spectra of a-Ge and LC-Ge thin films and c-Ge for reference.

For uniaxial stress along (110), the k_{TO} is about 3.10 cm^{-1}. A laser fluence of 110 mJ/cm^2 gives a Raman peak position at 297 cm^{-1}, whereas bulk c-Ge gives 300 cm^{-1}. For this reason, the stress over the grains is determined to be tensile, which corresponds to the shift of -3 cm^{-1} in the Raman peak for the sample irradiated with 110 mJ/cm^2. The value of σ is positive; therefore, the stress over the grains is determined to be tensile. The value of the tensile stress changes between 0.97 and 1.32 GPa. The effects of local heating are included in the improved phonon confinement model are correct for a broad range of Ge nanocrystal sizes from 1.3 to

10 nm. The effects of local heating, causing the red shift, are dominant at the size of ~5 nm for crystallites, where as the dominant cause of the red shift is caused by the tensile stress [63], [65], [66].

The linewidth of the LC-Ge because of several effects such as defect formations, the size of crystallites and the strain taking place during the solidification and crystallization phases. During the solidification phase, a significant number of defects form in the LC-Ge sample [77], [78], most likely due to diffusion of impurities from the glass substrate and the formation of inclusions and vacancies. The longer heating and melting times give increase to substantial parasitic diffusion of volatile atomic species such as Na, Mg and so on from the glass into molten Ge due to the effective increase of the local temperature under the molten Ge. In contrast, an abrupt solidification as in the case of EC leads to freezing and trapping of the impurities and an increase in the number of interstitials and vacancies. This defect-rich nature of the LC-Ge film can be avoided by several measures. First, incorporation of intermediate diffusion barrier layers between the glass substrate and the Ge film can limit the diffusion of the impurities from the substrate, and moreover, they may act as adhesion layers. Second, post-crystallization laser treatment at lower fluences can be effective in thermal curing and the removal of interstitial Ge and vacancies from LC-Ge.

4.2.2.3 EBSD Images and Grain Size Distribution

The crystal orientation and crystal size of LC-Ge is examined by electron back scatter diffraction (EBSD) measurements. EBSD images are obtained from the LC processed regions with non-overlapping and highly overlapping line focus pulses. Fig. 4.8 shows EBSD maps of LC regions induced by a single laser pulse (Fig. 4.8(a)) and successively overlapping laser pulses (Fig. 4.8(b)).

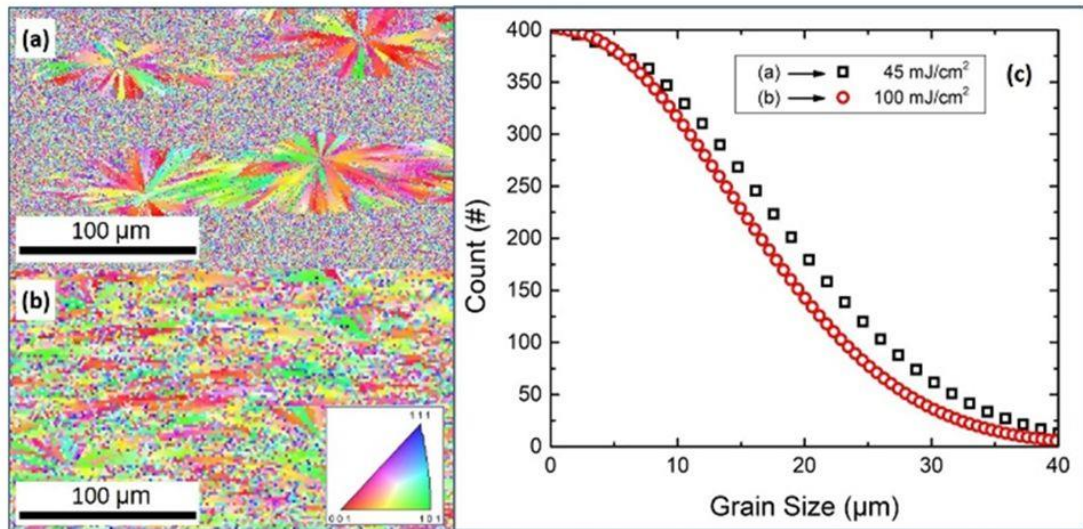

Figure 4.8 EBSD maps of the LC processed regions with laser fluences of (a) 45mJ/cm^2, (b) 110 mJ/cm^2 with color map and (c) the grain size distribution of 45 mJ/cm^2 and 110 mJ/cm^2.

The overlap ration of pulse is 99.9% which corresponds to a scan speed of 5 mm/s. The color map of EBSD shows the crystal direction or orientation. In Fig. 4.8(a) the surrounding local LC region is observed by a single laser pulse to have the form of a radially extending fan-like domain structure. As the heat diffusion through the film is negligible during the laser irradiation time, the heat produced by crystallization increases the temperature of the amorphous-crystalline interface easily [79].

When the EC is initiated, and crystal domains of tens of micrometers in size are achieved. In detail, the EC phenomenon is initiated by an instantaneous process such as laser irradiation [80]. Bensahel *et al.* have also shown that a CW laser irradiation of wavelength and fluence can induce EC of a 300 nm a-Ge film deposited by vacuum evaporation on quartz substrates. Bensahel *et al*. have confirmed that the self-thermal enhancement induces a self-sustained crystallization leading to the formation of a liquid region and surface damage. Unlike a liquid-solid interface, the nucleation region has a finite extent. The nucleation rate is low in a-Ge in CW laser experiments. The EC must be initiated by the local melting of the film [47]. Microstructures start from a random nucleus within a single pulse and extend radially

outwards generating fan-like neighbouring microcrystalline domains with random orientations, as can be seen in Fig. 4.7(a). Ortiz *et al*. have also observed similar fan-like structures consisting of radially extending crystallites in the EC [45]. It can be observed that the fan-like EC regions are in elliptical shape rather than circular with their long axis oriented along the axis of the line focus. This is due to the strong dependence of EC on the temperature gradient of the film [81]. The EC preferentially extends longer towards the lowest temperature gradient which is naturally along the long axis of our line focus. This observation also supports our suggestion that the fan-like crystalline domain layout is essentially since the EC regime is attained with our LC parameters. EBSD map shown in Fig. 4.8(a) (single pulse LC) exhibits inhomogeneous microstructures, where the sizes of these microstructures vary from 2 μm to 25 μm. EBSD map in Fig. 4.8(b) (overlap scan LC), in contrast, exhibits homogeneous microstructures, where the LC process switches to a different regime than EC. This mode can be defined as a slow quenching phase transition where the LC process takes place in a more controlled manner in film temperature than that of the EC. The average size of microstructures in Fig. 4.8(a) is 15 μm where the heat accumulation occurs and is maintained by the latent heat release. Crystallite growth is partially sustained at random locations where nucleation starts, and the accompanied latent heat release maintains the EC growth in the nearby vicinity. In high pulse overlap (Fig. 4.8(b)), the laser induced crystallization initiates while slow quenching of the surface is sustained. Hence the EC process switches to a slower LC process when the pulses are highly overlapped. The average size of homogeneous structures yields about 10 μm in this regime. On the one hand, the size of microstructures is shorter in the single pulse EC regime than the slow quenching high overlap regime. On the other hand, the microstructures are distributed more homogeneously over the entire film. Here, with increasing laser fluence, radially extending crystal domains overlap more to form a continuous microcrystalline network primarily composed of elongated crystallite domains. Unlike the spot focus, wider pc-Ge films were created by the overlapping line focus pulses (see Fig. 4.8(c)).

4.2.2.4 XRD Spectrum

A representative XRD spectrum of an LC sample of 110 mJ/cm^2 laser fluence and 5 mm/s scan speed is given in Fig. 4.9.

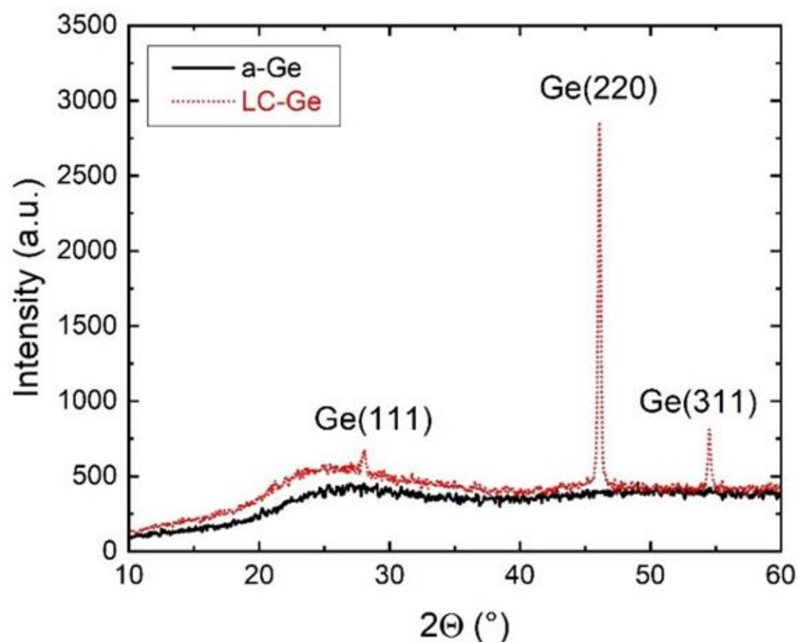

Figure 4.9 The XRD patterns of the as-deposited and LC-Ge thin-films at laser fluences of 110 mJ/cm^2.

According to the Raman measurements, there is no crystalline Ge formation in the XRD measurement of as-deposited reference film, indicating a completely amorphous phase of the unprocessed films. The LC-Ge film shows three peaks at positions 27°, 46°, and 54° corresponding to the (111), (220), and (311) planes of the expected diamond cubic crystal phase of Ge proving the presence of LC. The peak at 46° corresponding to the diffraction from the (220) plane is the strongest in terms of intensity compared to other planes in a ratio of (111) : (220) : (311) as 0.11 : 1.00 : 0.12. Based on the XRD results, the LC-Ge film is found to be preferentially oriented to (220) direction. In solid phase and metal induced crystallization processes, Ge films are preferentially grown in the (111) orientation due to the

energetically more stable and favourable configuration of this surface with a lower free energy than other orientations [30]. The diffraction peak of (220) plane, however, is commonly observed in crystallized Ge thin-films with moderate grain sizes where the diffraction peak of (111) plane is mostly observed from pc-Ge films with considerably larger grains [31]. The XRD results clearly reveal the Ge phase transition from amorphous to crystalline as a result of laser treatment which plays a critical role in driving the Ge atoms into the nucleation sites. Therefore, the crystallization of Ge films is limited by the mobility of the Ge atoms.

Raman spectroscopy results have revealed tensile strain in the processed films. However, XRD results here show that the films are strained compressively which indicates that the stress is inhomogeneously distributed over the films with compressive one being the dominant effect. Shifting of the XRD peaks towards higher 2θ values is attributed to the compressive stress throughout the crystalline regions. The crystal Ge with the stress-free lattice orientation (220) gives XRD signal at almost 45° [32], [33]. This is attributed to the bowing effect in the film during crystallization resulting in the surface of the film to be under moderate tensile and the substrate interface to be under a strong compressive strain as sketched in Fig. 4.10.

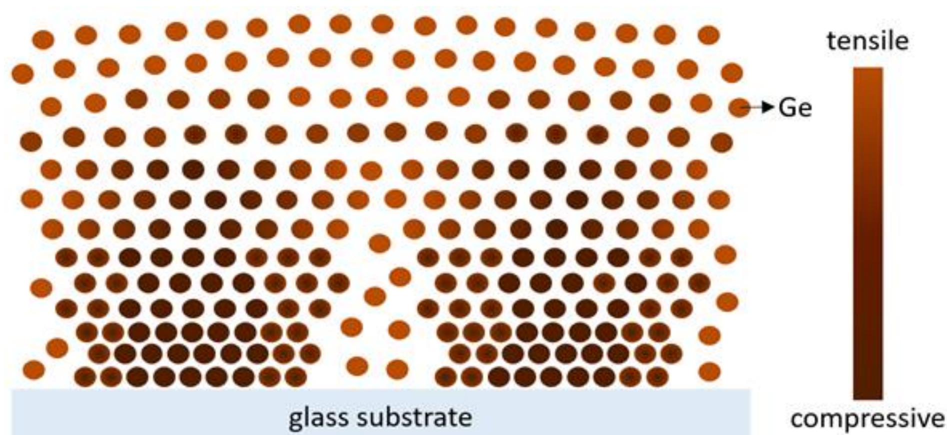

Figure 4.10 The bowing effect and differently stressed regions of LC Ge film.

4.2.2.5 Absorbance Spectrum

The measured absorbance spectra of a-Ge and LC-Ge films are shown in Figure 4.11.

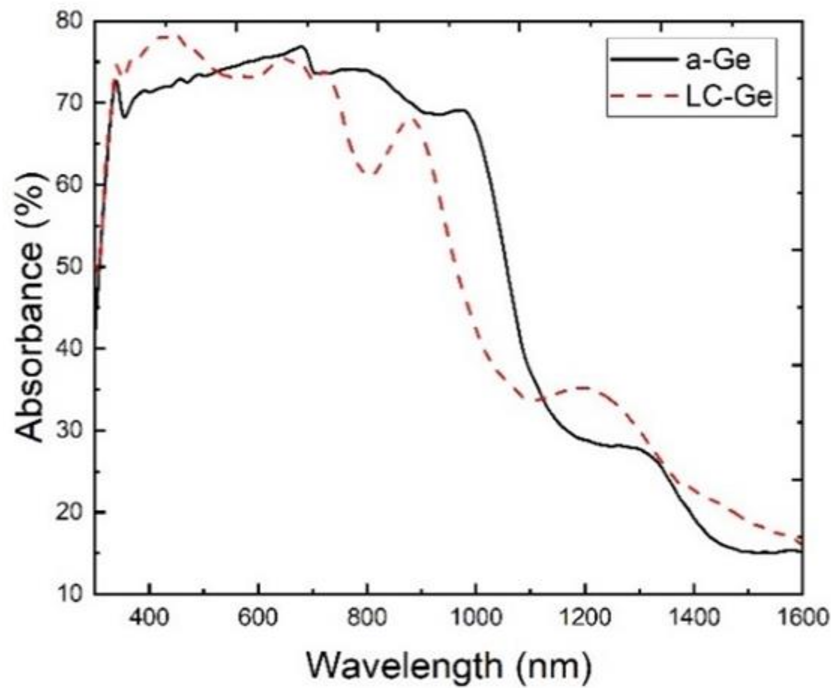

Figure 4.11 The absorbance spectrum of a-Ge and LC-Ge thin-films with a thickness of 300 nm.

The optical absorbance of the glass substrate is subtracted from the total absorbance of the samples to deduce the absorbance solely due to the films in both cases. The absorbance spectrum of a-Ge has a sharper transition than that of LC-Ge, which is due to the structural modification of the surface after the LC process (see Fig. 4.11). The surface homogeneity of the LC processed region is not as high as the as-deposited a-Ge; hence there are fluctuations. Moreover, the reflectance of LC-Ge is higher than the a-Ge [82].

CHAPTER 5

LASER CRYSTALLIZATION AND CHARACTERIZATION OF AMORPHOUS GERMANIUM THIN-FILMS DEPOSITED BY RF SPUTTERING

300 nm thick a-Ge thin films on glass substrate are prepared by an electron-beam evaporator. In this chapter, the processed LC-Ge thin-films are characterized using Raman spectroscopy, optical microscopy and EBSD.

5.1 Preparation of a-Ge Thin-Films

a-Ge with a thickness of 300 nm is deposited by radio-frequency (RF) magnetron sputtering on glass substrate. Deposition parameters are set as 200W RF power, 2mTorr deposition pressure and 20 sccm argon gas flow rate where the base pressure is approximately 1.1x10-6 Torr.

5.2 Laser Crystallization of a-Ge Thin-Films and Line Focus Scanning by the Cylindrical Lens

300 nm thick a-Ge thin-films on glass substrate that was deposited by RF sputtering are processed with the close value of laser fluences and scan speeds with the 300 nm thick a-Ge thin-films on glass substrate that was deposited by e-beam deposition. The LC was performed at a fixed scan speed of 5 mm/s with laser fluences 53, 68 and 82 mJ/cm^2. Laser fluences below 53 mJ/cm^2 at 5 mm/s scan speed are found not to be sufficient to induce melting.

5.2.1 Optical Microscope, EBSD, SEM and Raman Measurement Results

The optical microscope and SEM images of the LC-processed regions with laser fluences of 53 mJ/cm^2 and scan speed of 5 mm/s in Figure 5.1. In the sample process

with a laser fluence of 53 mJ/cm^2 in Figure 5.1.(a), laser pulses are not distributed on the surface homogeneously. The crystallites are grown in the way bending.

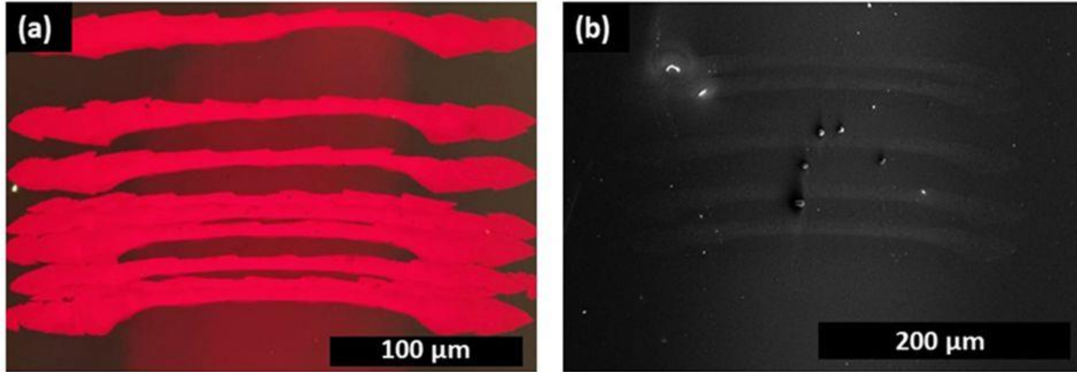

Figure 5.1 Optical microscope and SEM image of the LC-processed regions with the laser fluences of 53 mJ/cm^2 and scan speed of 5 mm/s.

During the laser crystallization, damage appears at the centre of the LC-processed region in Fig. 5.2. The laser fluence profile of a Gaussian beam is maximum at the centre; therefore, the damage region can be seen. The width of the crystallized domains is strongly related with the width of the line focus of the beam and spatial homogeneity of its fluence distribution.

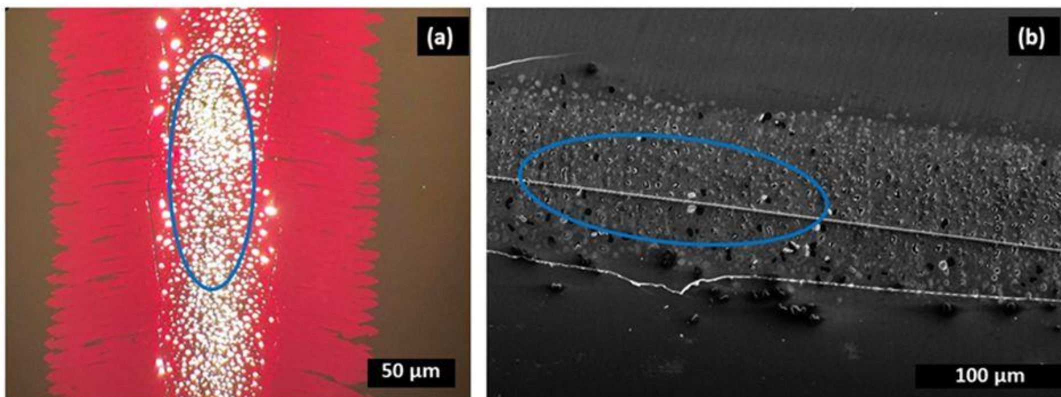

Figure 5.2 Optical microscope and SEM image of the LC-processed regions with the laser fluences of 82 mJ/cm^2 and scan speed of 5 mm/s.

Raman spectroscopy is used to determine the type of the stress on the Ge films after the laser irradiation. The Raman spectra of LC-Ge regions irradiated by the cylindrical lens, as shown in Fig. 5.3. The Raman signal is collected using the Andor SR750 spectrometer and Verdi V-6 laser system with a wavelength of 532 nm. The excitation power is 50 mW on the sample surface and 17 µm spot size as excitation source. The LC-Ge Raman peak is redshifted by 8 cm^{-1} as compared to that of the bulk-Ge (300 cm^{-1}), which designates presence of tensile stress throughout the film surface.

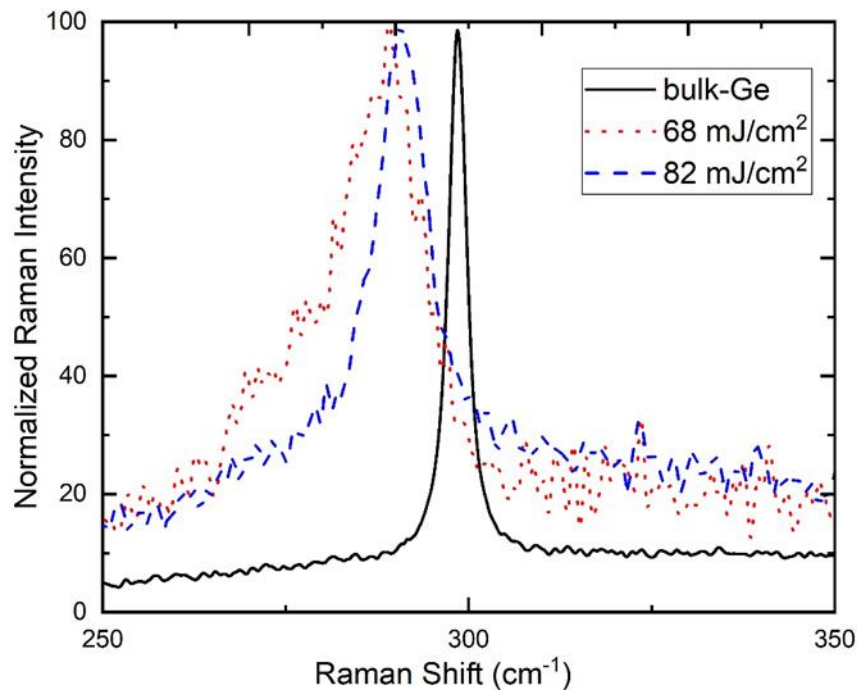

Figure 5.3 Raman spectra of the bulk-Ge and the LC-processed samples with laser fluences of 68 mJ/cm^2 and 82 mJ/cm^2 with the scan speed of 5 mm/s.

The optical microscope and EBSD images of the LC-processed regions with laser fluences of 68 mJ/cm^2 and scan speed of 5 mm/s in Fig. 5.4. The length of pc-Ge grains is about 30 µm.

Figure 5.4 Optical microscope images of LC processed sputtered Ge region using (a) the cylindrical lens (b) their corresponding EBSD maps.

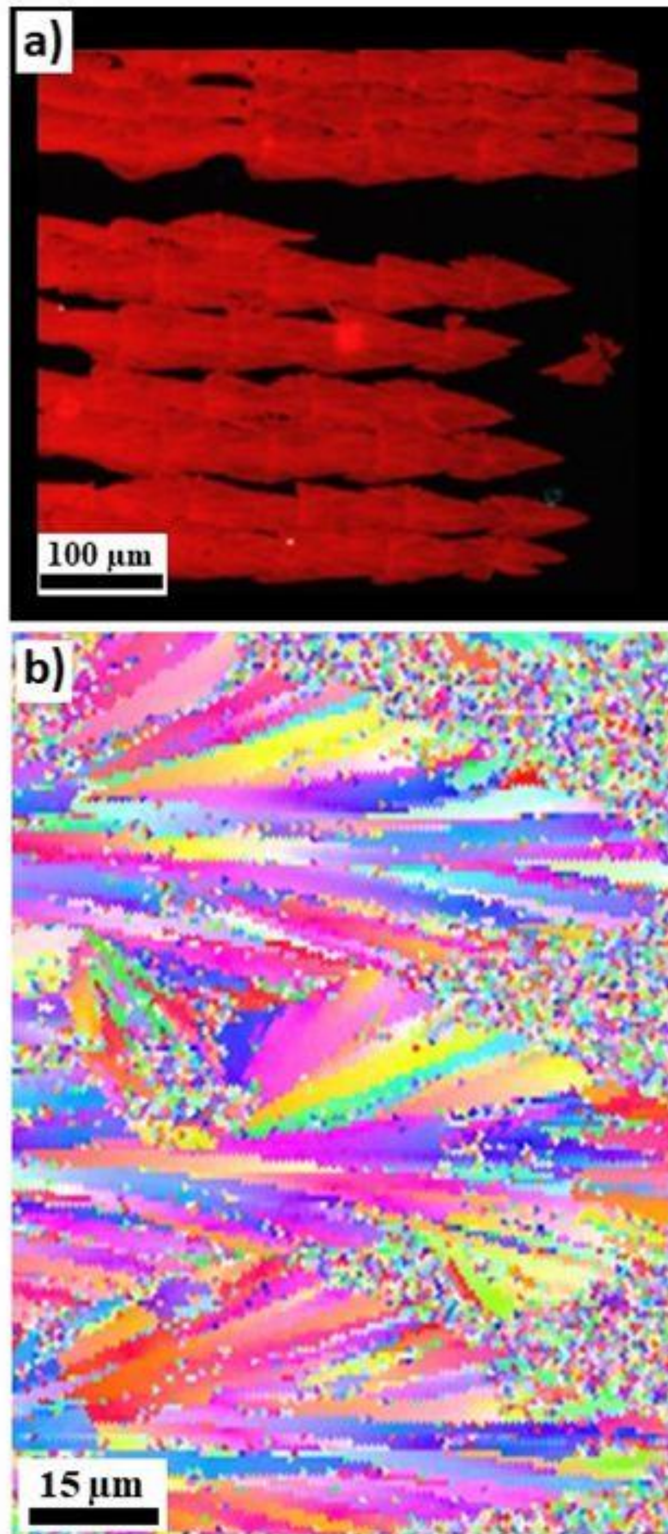

5.3 Laser Crystallization of a-Ge Thin-Films and Line Focus Scanning by the Powell Lens

The laser beam was focused on the film surface by a telecentric lens after passing through a 2-D galvo-mirror set at a distance of 182 mm. The Powell lens has 6.30 mm apex length and 30º fan angle. The beam profile is flat-top. It focuses the beam with dimensions of 45×3250 μm. To achieve wider scanning area, the Powell lens is integrated to the laser system. 3 mm beam width of the Powell lens, compared to the 1 mm width of the cylindrical lens, results in wider scanning area. The Powell lens offers to transform the Gaussian beam into a flat-top beam [83].

5.3.1 Optical Microscope, SEM and EBSD Measurement Results

LC was performed at a fixed scan speed of 5 mm/s with laser fluences 54, 68 and 72 mJ/cm^2. The optical microscope and EBSD images of the LC-Ge region with a laser fluence of 54 mJ/cm^2 with a scan speed of 5 mm is shown in Figure 5.5.

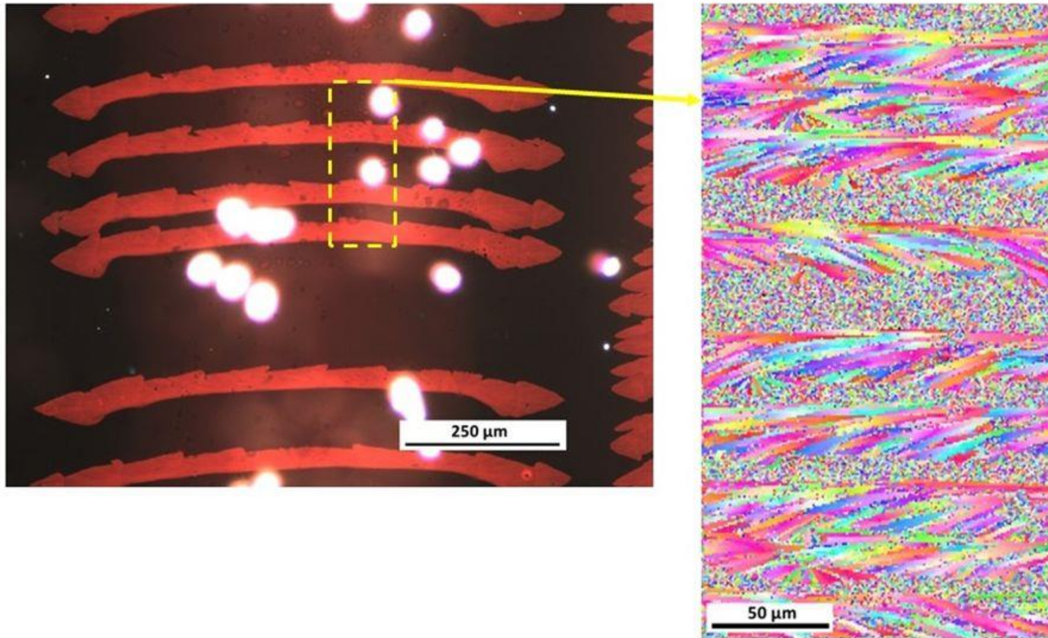

Figure 5.5 Optical microscope and EBSD images of the LC-Ge with a laser fluence of 54 mJ/cm^2 and a scan speed of 5 mm/s, respectively.

The SEM and EBSD images of the LC-Ge region with a laser fluence of 68 mJ/cm^2 with a scan speed of 5 mm/s is shown in Figure 5.6. It is seen from the EBSD images that the grain sizes are increased up to 50 µm by means of applying more fluence with more overlapping line focus pulses (see Figure 5.6).

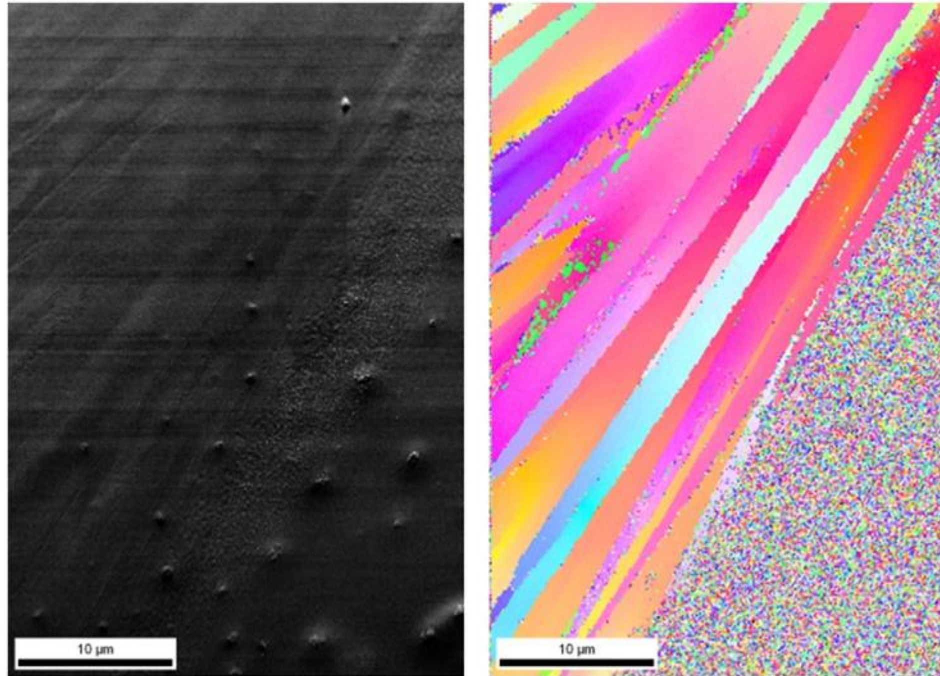

Figure 5.6 SEM and EBSD images of the LC-Ge with a laser fluence of 68 mJ/cm^2 and a scan speed of 5 mm/s, respectively.

The SEM and EBSD images of the LC-Ge region with a laser fluence of 72 mJ/cm^2 with a scan speed of 5 mm/s is shown in Figure 5.7. The length of pc-Ge grains which achieved by the Powell lens is 50 µm, as seen in Fig. 5.7.

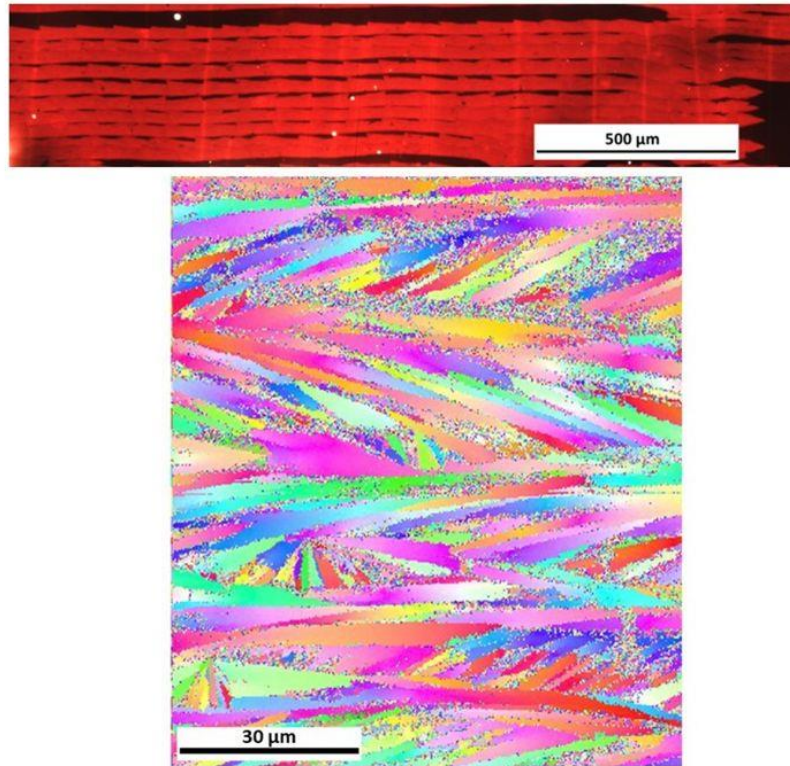

Figure 5.7 SEM and EBSD images of the LC-Ge with a laser fluence of 72 mJ/cm^2 and a scan speed of 5 mm/s, respectively.

The crystal domain orientation using the Powell lens is observed to elongate laterally, resulting in much longer grain sizes in comparison with the cylindrical lens. The Powell lens converts the incoming Gaussian laser beam into a homogeneous flat-top beam; thus, thermal gradient can be maintained through the growth of the crystal domain.

CHAPTER 6

CONCLUSION AND FUTURE WORK

In this thesis, laser crystallization of a-Ge thin films on a solar glass substrate is investigated in a controllable manner using a nanosecond pulsed IR laser with a line focus. The highly overlapping of the line focus laser with a cylindrical lens create microcrystallites with an average size of 15 μm where the line focus with a powell lens create microcrystallites with an average size of 30 μm. A cylindrical lens is utilized to expand the spot focus into a line focus. 3 mm beam width of the Powell lens, compared to the 1 mm width of the cylindrical lens, results in wider scanning area. For achieving a wider scanning area, only an increase in the average power equal to the increase in the focal line length will be sufficient. Moreover, the Powell lens generates a laser profile with a more uniform energy distrubution. The red shift of Raman peaks is attributed to the tensile stress throughout the film surface. Considering the distribution density of Ge crystal domains, the density of crystalline materials is higher than the density of amorphous materials, and crystallization may cause some stretching of the crystals. The crystallites with dimensions greater than 100 nm can consist of slightly misoriented nanocrystals. These crystallites can contain structural defects and may experience stretching strains. The crystal quality is preserved throughout the 300 nm thick film, even on the glass substrate. The dynamics of single-pulse LC of a-Ge to be EC and that of high-overlap pulse scan LC to be of a slow-quenching crystallization nature based on the crystal domain orientation and their elongated fan-like radial lateral organization is explained. Successful crystallization of a-Ge thin-film is confirmed by optical microscopy, Raman spectroscopy, SEM, EBSD and XRD measurements. LC-Ge is mostly oriented to the (220) direction. According to EBSD maps, the microcrystallites are formed inhomogeneously when the film is processed at the crystallization threshold laser fluence where the high-aspect microcrystal grains extend radially outward from random nucleation centers, as expected from EC. When the laser fluence is

approximately twice the crystallization threshold, more homogeneous distribution of the microcrystallite grains due to the attainment of slow quenching yielding a more controlled processing regime is observed. When the laser fluence approaches a value that is just at the damage threshold of the film, the lengths of the grains reach their potential maximum length. According to the results of Raman spectroscopy, a tensile strain of ~ 1.3 GPa exists on the film surface. Besides a small amount of residual stress, the peak position and peak width of LC-Ge films are close to that of bulk c-Ge. Raman analysis results based on the presence of microcrystalline domains, as evidenced from EBSD measurements. This should not exclude the possibility of a broader-scope Raman analysis which may, for instance, take into account phonon confinement effects, as exhibited by nanocrystalline Ge assuming its coexistence with microcrystalline Ge. Furthermore, microcrystal grain sizes can be increased laterally by careful adjustment of the line focus geometry. Moderation of the temperature gradient in the laser-irradiated film by the help of high-aspect ellipticity of the focal spot in the line-focus configuration is shown to play a role in the elongation of the microcrystal domains. This study demonstrates that different deposition techniques and focal spot geometries affect the crystal grains growth. The LC of sputtered a-Ge gives rise to grain lengths about 40 µm longer than the deposited e-beam. Modifying the line focus system with the Powell lens, 1 cm^2 area is processed 5 times faster. These findings pave the way for producing crack-free and high-quality crystalline device-grade thin-films, which may find applications in photovoltaics, and other thin-film device applications. As future work, the sputtered amorphous Ge microstructures can be crystallized with a ns pulsed IR laser with a suitable laser parameters.

REFERENCES

[1] S. Adachi, *Optical Constants of Crystalline and Amorphous Semiconductors*. 1999.

[2] R. Soref, “Mid-infrared photonics in silicon and germanium,” *Nat. Photonics*, vol. 4, no. 8, pp. 495–497, 2010, doi: 10.1038/nphoton.2010.171.

[3] L. Zhang, A. M. Agarwal, L. C. Kimerling, and J. Michel, “Nonlinear Group IV photonics based on silicon and germanium: From near-infrared to mid-infrared,” *Nanophotonics*, vol. 3, no. 4–5, pp. 247–268, 2014, doi: 10.1515/nanoph-2013-0020.

[4] E. E. Haller, “Germanium: From its discovery to SiGe devices,” *Mater. Sci. Semicond. Process.*, vol. 9, no. 4-5 SPEC. ISS., pp. 408–422, 2006, doi: 10.1016/j.mssp.2006.08.063.

[5] M. L. Lee, E. A. Fitzgerald, M. T. Bulsara, M. T. Currie, and A. Lochtefeld, “Strained Si, SiGe, and Ge channels for high-mobility metal-oxide-semiconductor field-effect transistors,” *J. Appl. Phys.*, vol. 97, no. 1, 2005, doi: 10.1063/1.1819976.

[6] K. L. Chopra and S. K. Bahl, “Structural, electrical, and optical properties of amorphous germanium films,” *Phys. Rev. B*, vol. 1, no. 6, pp. 2545–2556, 1970, doi: 10.1103/PhysRevB.1.2545.

[7] S. J. Koester, J. D. Schaub, G. Dehlinger, and J. O. Chu, “Germanium-on-SOI infrared detectors for integrated photonic applications,” *IEEE J. Sel. Top. Quantum Electron.*, vol. 12, no. 6, pp. 1489–1502, 2006, doi: 10.1109/JSTQE.2006.883160.

[8] F. T. Si, O. Isabella, and M. Zeman, “Thin-film amorphous silicon germanium solar cells with p- and n-type hydrogenated silicon oxide layers,” *Sol. Energy Mater. Sol. Cells*, vol. 163, no. January, pp. 9–14, 2017, doi: 10.1016/j.solmat.2017.01.001.

[9] D. Marris-Morini *et al.*, “Low energy consumption and high speed germanium-based optoelectronic devices,” *2013 Conf. Lasers Electro-Optics Eur. Int. Quantum Electron. Conf. CLEO/Europe-IQEC 2013*, vol. 3224, no. 2012, p. 141106, 2013, doi: 10.1109/CLEOE-IQEC.2013.6801255.

[10] C. Z. Fang *et al.*, “Germanium-tin alloys: Applications for optoelectronics in mid-infrared spectra,” *Opto-Electronic Adv.*, vol. 1, no. 3, pp. 1–10, 2018, doi: 10.29026/oea.2018.180004.

[11] “Levinshtein, Rumyantsev, Shur_1996_Handbook Series on Semiconductor Parameters, vol. 1.pdf.” .

[12] J. Fernandez, “Development of Crystalline Germanium for Thermophotovoltaics and High-Efficiency Multi-Junction Solar Cells,” p. 152, 2010.

[13] A. A. Akl and H. Howari, “Nanocrystalline formation and optical properties of germanium thin films prepared by physical vapor deposition,” *J. Phys. Chem. Solids*, vol. 70, no. 10, pp. 1337–1343, 2009, doi: 10.1016/j.jpcs.2009.07.016.

[14] K. Çinar, M. Karaman, and A. Bek, “Improvement of Laser-Crystallized Silicon Film Quality via Intermediate Dielectric Layers on a Glass Substrate,” *ACS Omega*, vol. 3, no. 5, pp. 5846–5852, 2018, doi: 10.1021/acsomega.8b00530.

[15] D. Eisenhauer *et al.*, “Smooth anti-reflective three-dimensional textures for liquid phase crystallized silicon thin-film solar cells on glass,” *Sci. Rep.*, 2017, doi: 10.1038/s41598-017-02874-y.

[16] K. Jäger *et al.*, “Simulations of sinusoidal nanotextures for coupling light into c-Si thin-film solar cells,” *Opt. Express*, 2016, doi: 10.1364/oe.24.00a569.

[17] G. Köppel, D. Eisenhauer, B. Rech, and C. Becker, “Combining tailor-made textures for light in-coupling and light trapping in liquid phase crystallized silicon thin-film solar cells,” *Opt. Express*, 2017, doi: 10.1364/oe.25.00a467.

[18] V. Preidel, D. Amkreutz, J. Haschke, M. Wollgarten, B. Rech, and C. Becker, "Balance of optical, structural, and electrical properties of textured liquid phase crystallized Si solar cells," *J. Appl. Phys.*, 2015, doi: 10.1063/1.4922138.

[19] I. Kabacelik, M. Kulakci, and R. Turan, "Structural and electrical analysis of poly-Ge films fabricated by e-beam evaporation for optoelectronic applications," *Mater. Sci. Semicond. Process.*, vol. 56, no. August, pp. 368–372, 2016, doi: 10.1016/j.mssp.2016.09.023.

[20] I. Kabacelik, M. Kulakci, and R. Turan, "Investigation of silver-induced crystallization of germanium thin films fabricated on different substrates," *J. Cryst. Growth*, vol. 419, pp. 7–11, 2015, doi: 10.1016/j.jcrysgro.2015.02.078.

[21] K. Sakaike, S. Higashi, H. Murakami, and S. Miyazaki, "Crystallization of amorphous Ge films induced by semiconductor diode laser annealing," *Thin Solid Films*, vol. 516, no. 11, pp. 3595–3600, 2008, doi: 10.1016/j.tsf.2007.08.028.

[22] O. Salihoglu, U. Kürüm, H. Gul Yaglioglu, A. Elmali, and A. Aydinli, "Femtosecond laser crystallization of amorphous Ge," *J. Appl. Phys.*, vol. 109, no. 12, 2011, doi: 10.1063/1.3601356.

[23] T. T. Li, L. B. Bayu Aji, T. W. Heo, M. K. Santala, S. O. Kucheyev, and G. H. Campbell, "Effect of medium range order on pulsed laser crystallization of amorphous germanium thin films," *Appl. Phys. Lett.*, vol. 108, no. 22, 2016, doi: 10.1063/1.4953153.

[24] J. Zhang *et al.*, "Modeling of continuous wave laser melting of germanium epitaxial films on silicon substrates," *Mater. Express*, 2017, doi: 10.1166/MEX.2017.1382.

[25] W. Yeh, H. Chen, H. Huang, C. Hsiao, and J. Jeng, "Superlateral growth of a-Ge film by excimer laser annealing," *Appl. Phys. Lett.*, vol. 93, no. 9, pp. 10–13, 2008, doi: 10.1063/1.2977965.

[26] F. Falk and G. Andrä, “Laser crystallization - A way to produce crystalline silicon films on glass or on polymer substrates,” 2006, doi: 10.1016/j.jcrysgro.2005.11.052.

[27] M. Mulato, D. Toet, G. Aichmayr, P. V. Santos, and I. Chambouleyron, “Short-pulse laser-induced crystallization of intrinsic and hydrogenated amorphous germanium thin films,” *J. Appl. Phys.*, vol. 82, no. 10, pp. 5159–5166, 1997, doi: 10.1063/1.366320.

[28] M. Mulato, D. Toet, G. Aichmayr, P. V. Santos, and I. Chambouleyron, “Laser crystallization and structuring of amorphous germanium,” *Appl. Phys. Lett.*, vol. 70, no. 26, pp. 3570–3572, 1997, doi: 10.1063/1.119236.

[29] A. H. Hamad, “Effects of Different Laser Pulse Regimes (Nanosecond, Picosecond and Femtosecond) on the Ablation of Materials for Production of Nanoparticles in Liquid Solution,” *High Energy Short Pulse Lasers*, 2016, doi: 10.5772/63892.

[30] S. Hu, A. F. Marshall, and P. C. McIntyre, “Interface-controlled layer exchange in metal-induced crystallization of germanium thin films,” *Appl. Phys. Lett.*, vol. 97, no. 8, pp. 1–4, 2010, doi: 10.1063/1.3480600.

[31] C. Y. Tsao, J. W. Weber, P. Campbell, P. I. Widenborg, D. Song, and M. A. Green, “Low-temperature growth of polycrystalline Ge thin film on glass by in situ deposition and ex situ solid-phase crystallization for photovoltaic applications,” *Appl. Surf. Sci.*, vol. 255, no. 15, pp. 7028–7035, 2009, doi: 10.1016/j.apsusc.2009.03.035.

[32] S. Goriparti *et al.*, “Germanium Nanocrystals-MWCNTs Composites as Anode Materials for Lithium Ion Batteries,” *ECS Trans.*, vol. 62, no. 1, pp. 19–24, 2014, doi: 10.1149/06201.0019ecst.

[33] W. J. Shi, Y. Y. Yi, and M. Li, “Pressure dependence of refractive index of Ge near the absorption edge,” *Wuli Xuebao/Acta Phys. Sin.*, vol. 65, no. 16, 2016, doi: 10.7498/aps.65.167801.

[34] P. Nath and K. L. Chopra, "Thermal conductivity of amorphous and crystalline Ge and GeTe films," *Phys. Rev. B*, vol. 10, no. 8, pp. 3412–3418, 1974, doi: 10.1103/PhysRevB.10.3412.

[35] "In situ observation of laser induced crystallisation in group IV semiconductors."

[36] A. Chojnacka and M. O. Thompson, "Morphological instabilities during explosive crystallization of germanium films," *Mater. Res. Soc. Symp. - Proc.*, vol. 648, pp. 1–8, 2001, doi: 10.1557/proc-648-p11.12.

[37] C. Grigoropoulos, M. Rogers, S. H. Ko, A. A. Golovin, and B. J. Matkowsky, "Explosive crystallization in the presence of melting," *Phys. Rev. B - Condens. Matter Mater. Phys.*, vol. 73, no. 18, 2006, doi: 10.1103/PhysRevB.73.184125.

[38] P. Baeri, S. U. Campisano, G. Foti, and E. Rimini, "A melting model for pulsing-laser annealing of implanted semiconductors," *J. Appl. Phys.*, vol. 50, no. 2, pp. 788–797, 1979, doi: 10.1063/1.326046.

[39] P. Chaudhari, "Grain Growth and Stress Relief in Thin Films," *J. Vac. Sci. Technol.*, vol. 9, no. 1, pp. 520–522, 1972, doi: 10.1116/1.1316674.

[40] A. A. Grinberg, R. F. Mekhtiev, S. M. Ryvkin, V. M. Salmanov, and I. D. Yaroshetskii, "Absorption of laser radiation and damage in semiconductors," *Sov. Phys. - Solid State*, vol. 9, no. 5, pp. 1085–1090, 1967.

[41] R. F. Wood and G. E. Giles, "Macroscopic theory of pulsed-laser annealing. I. Thermal transport and melting," *Phys. Rev. B*, 1981, doi: 10.1103/PhysRevB.23.2923.

[42] Norbert H. Nickel, "Laser Crystallization of Silicon," *Elsevier*, 2003.

[43] Y. Il Son and J. Shin, "Numerical Study on the Laser Annealing of Silicon Used in Advanced V-NAND Device," *Materials (Basel).*, vol. 15, no. 12, pp. 1–13, 2022, doi: 10.3390/ma15124201.

[44] R. Černý and P. Přikryl, “Nonequilibrium model of laser-induced phase change processes in amorphous silicon thin films,” *Phys. Rev. B - Condens. Matter Mater. Phys.*, vol. 57, no. 1, pp. 194–202, 1998, doi: 10.1103/PhysRevB.57.194.

[45] C. Ortiz, K. A. Rubin, and S. A. Iuria, “Laser-Induced Multi-Crystallization of Thin Germanium Films,” *MRS Proc.*, vol. 129, pp. 455–460, 1988, doi: 10.1557/proc-129-455.

[46] M. Okugawa, R. Nakamura, H. Numakura, A. Heya, N. Matsuo, and H. Yasuda, “The relation between amorphous structure and explosive crystallization of sputter-deposited amorphous germanium thin films,” *Jpn. J. Appl. Phys.*, vol. 58, no. 4, 2019, doi: 10.7567/1347-4065/ab0909.

[47] H. J. Leamy, W. L. Brown, G. K. Celler, G. Foti, G. H. Gilmer, and J. C. C. Fan, “Explosive crystallization of amorphous germanium,” *Appl. Phys. Lett.*, vol. 38, no. 3, pp. 137–139, 1981, doi: 10.1063/1.92277.

[48] J. C. C. Fan and H. J. Zeiger, “Crystallization of amorphous silicon films by Nd:YAG laser heating,” *Appl. Phys. Lett.*, 1975, doi: 10.1063/1.88437.

[49] P. Pierrard, B. Mutaftschiev, W. Marine, J. Marfaing, and F. Salvan, “In situ crystallization of amorphous germanium under laser irradiation in a transmission electron microscope,” *Thin Solid Films*, 1984, doi: 10.1016/0040-6090(84)90482-6.

[50] C. Wilkins, “Fourier Transform Spectrometry By Sumner P. Davis (University of California, Berkeley), Mark C. Adams (ITT Industries Aerospace/Communicatons, Fort Wayne, Indiana), and James W. Brault (Formerly of National Solar Observatory, Kitt Peak, Arizona). Academic,” *J. Am. Chem. Soc.*, vol. 124, no. 19, pp. 5601–5601, 2002, doi: 10.1021/ja0153060.

[51] “What is Raman Spectroscopy?” https://www.edinst.com/blog/what-is-raman-spectroscopy/.

[52] M. Bauer, “Raman spectroscopy of laser induced material alterations,” pp. 1–128, 2010.

[53] V. Senez *et al.*, “Strain determination in silicon microstructures by combined convergent beam electron diffraction, process simulation, and micro-Raman spectroscopy,” *J. Appl. Phys.*, vol. 94, no. 9, pp. 5574–5583, 2003, doi: 10.1063/1.1611287.

[54] S. M. Hu, “Stress-related problems in silicon technology,” *J. Appl. Phys.*, vol. 70, no. 6, 1991, doi: 10.1063/1.349282.

[55] J. Menéndez and M. Cardona, “Temperature dependence of the first-order Raman scattering by phonons in Si, Ge, and -Sn: Anharmonic effects,” *Phys. Rev. B*, vol. 29, no. 4, pp. 2051–2059, 1984, doi: 10.1103/PhysRevB.29.2051.

[56] P. Lengsfeld, N. H. Nickel, C. Genzel, and W. Fuhs, “Stress in undoped and doped laser crystallized poly-Si,” *J. Appl. Phys.*, vol. 91, no. 11, pp. 9128–9135, 2002, doi: 10.1063/1.1476083.

[57] I. De Wolf, “Micro-Raman spectroscopy to study local mechanical stress in silicon integrated circuits,” *Semicond. Sci. Technol.*, vol. 11, no. 2, pp. 139–154, 1996, doi: 10.1088/0268-1242/11/2/001.

[58] K. Dombrowski, “Micro-Raman investigation of mechanical stress in Si devise structures and phonons in SiGe /,” 2007.

[59] G. Lucazeau, “Effect of pressure and temperature on Raman spectra of solids: Anharmonicity,” *J. Raman Spectrosc.*, vol. 34, no. 7–8, pp. 478–496, 2003, doi: 10.1002/jrs.1027.

[60] A. Gassenq *et al.*, “Raman-strain relations in highly strained Ge: Uniaxial ⟨100⟩, ⟨110⟩ and biaxial (001) stress,” *J. Appl. Phys.*, vol. 121, no. 5, 2017, doi: 10.1063/1.4974202.

[61] V. A. Volodin and D. I. Koshelev, “Quantitative analysis of hydrogen in amorphous silicon using Raman scattering spectroscopy,” *J. Raman*

Spectrosc., vol. 44, no. 12, pp. 1760–1764, 2013, doi: 10.1002/jrs.4408.

[62] V. A. Volodin, G. K. Krivyakin, G. D. Ivlev, S. L. Prokopyev, S. V. Gusakova, and A. A. Popov, "Crystallization of Amorphous Germanium Films and Multilayer a-Ge/a-Si Structures upon Exposure to Nanosecond Laser Radiation," *Semiconductors*, vol. 53, no. 3, pp. 400–405, 2019, doi: 10.1134/S1063782619030217.

[63] V. A. Volodin, D. V. Marin, V. A. Sachkov, E. B. Gorokhov, H. Rinnert, and M. Vergnat, "Applying an improved phonon confinement model to the analysis of Raman spectra of germanium nanocrystals," *J. Exp. Theor. Phys.*, vol. 118, no. 1, pp. 65–71, 2014, doi: 10.1134/S1063776114010208.

[64] Y. Maeda, "Visible photoluminescence from nanocrystallite Ge embedded in a glassy SiO2 matrix: Evidence in support of the quantum-confinement mechanism," *Phys. Rev. B*, vol. 51, no. 3, pp. 1658–1670, 1995, doi: 10.1103/PhysRevB.51.1658.

[65] K. Tani, K. Oda, and T. Ido, "Analysis of stress distribution in microfabricated germanium with external stressors for enhancement of light emission," *Opt. Express*, vol. 28, no. 25, p. 38267, 2020, doi: 10.1364/oe.413503.

[66] T. Imajo, T. Suemasu, and K. Toko, "Strain effects on polycrystalline germanium thin films," *Sci. Rep.*, vol. 11, no. 1, pp. 1–6, 2021, doi: 10.1038/s41598-021-87616-x.

[67] M. D. Efremov, V. V. Bolotov, V. A. Volodin, L. I. Fedina, and E. A. Lipatnikov, "Excimer laser and rapid thermal annealing stimulation of solid-phase nucleation and crystallization in amorphous silicon films on glass substrates," *J. Phys. Condens. Matter*, vol. 8, no. 3, pp. 273–286, 1996, doi: 10.1088/0953-8984/8/3/007.

[68] X. Wu, J. Yu, T. Ren, and L. Liu, "Micro-Raman spectroscopy measurement of stress in silicon," *Microelectronics J.*, vol. 38, no. 1, pp. 87–90, 2007, doi: 10.1016/j.mejo.2006.09.007.

[69] C. Georgi, M. Hecker, and E. Zschech, "Effects of laser-induced heating on Raman stress measurements of silicon and silicon-germanium structures," *J. Appl. Phys.*, vol. 101, no. 12, 2007, doi: 10.1063/1.2743882.

[70] Z. Hao, S. A. Kochubei, A. A. Popov, and V. A. Volodin, "On Raman scattering cross section ratio of amorphous to nanocrystalline germanium," *Solid State Commun.*, vol. 313, no. April, p. 113897, 2020, doi: 10.1016/j.ssc.2020.113897.

[71] S. Osswald, V. N. Mochalin, M. Havel, G. Yushin, and Y. Gogotsi, "Phonon confinement effects in the Raman spectrum of nanodiamond," *Phys. Rev. B - Condens. Matter Mater. Phys.*, vol. 80, no. 7, 2009, doi: 10.1103/PhysRevB.80.075419.

[72] A. Hohnholz, K. Rettschlag, M. Desens, P. A. Taschner, and L. Overmeyer, "Optics and Apparatus for CO2 and CO Laser Micro-processing," in *Handbook of Laser Micro- and Nano-Engineering*, K. Sugioka, Ed. Cham: Springer International Publishing, 2020, pp. 1–37.

[73] V. Türker, M. E. Yağcı, S. H. Salman, K. Çınar, S. K. Eken, and A. Bek, "A Dual-Wavelength Pulsed Laser Processing Platform for a-Si Thin Film Crystallization," *Instruments*, vol. 3, no. 2, p. 31, 2019, doi: 10.3390/instruments3020031.

[74] A. Farnia, F. Malek Ghaini, and J. Sabbaghzadeh, "Effects of pulse duration and overlapping factor on melting ratio in preplaced pulsed Nd:YAG laser cladding," *Opt. Lasers Eng.*, vol. 51, no. 1, pp. 69–76, 2013, doi: 10.1016/j.optlaseng.2012.07.015.

[75] C. Y. Peng *et al.*, "Comprehensive study of the Raman shifts of strained silicon and germanium," *J. Appl. Phys.*, vol. 105, no. 8, 2009, doi: 10.1063/1.3110184.

[76] D. M. Zhigunov, A. B. Evlyukhin, A. S. Shalin, U. Zywietz, and B. N. Chichkov, "Femtosecond Laser Printing of Single Ge and SiGe Nanoparticles

with Electric and Magnetic Optical Resonances," *ACS Photonics*, vol. 5, no. 3, pp. 977–983, 2018, doi: 10.1021/acsphotonics.7b01275.

[77] A. Wellner *et al.*, "Stress measurements of germanium nanocrystals embedded in silicon oxide," *J. Appl. Phys.*, 2003, doi: 10.1063/1.1617361.

[78] S. K. Gupta and P. K. Jha, "Modified phonon confinement model for size dependent Raman shift and linewidth of silicon nanocrystals," *Solid State Commun.*, 2009, doi: 10.1016/j.ssc.2009.08.036.

[79] P. Fontaine, J. Marfaing, W. Marine, F. Salvan, and B. Mutaftschiev, "Instabilities of Crystallization in Amorphous Germanium Under Pulsed Laser Irradiation.," pp. 19–24, 1984, doi: 10.1007/978-3-642-82381-7_3.

[80] D. Bensahel and G. Auvert, "Explosive Crystallization in a-Ge and a-Si: A Review," *MRS Online Proc. Libr.*, vol. 13, no. 1, pp. 165–176, 1982, doi: 10.1557/PROC-13-165.

[81] C. Césari, G. Nihoul, J. Marfaing, W. Marine, and B. Mutaftschiev, "Amorphous-crystalline interfaces after laser induced explosive crystallization in amorphous germanium," *Surf. Sci.*, 1985, doi: 10.1016/0039-6028(85)90972-0.

[82] F. Vega, R. Serna, C. N. Afonso, D. Bermejo, and G. Tejeda, "Relaxation and crystallization kinetics of amorphous germanium films by nanosecond laser pulses," *J. Appl. Phys.*, vol. 75, no. 11, pp. 7287–7291, 1994, doi: 10.1063/1.356663.

[83] O. Willstrand, "Intensity distribution conversion from Gaussian to Top-Hat in a single-mode fiber connector," *Lund Univ.*, vol. Master Thesis, 2013, [Online]. Available: http://lup.lub.lu.se/student-papers/record/3410933.